

Design of Calorimeter and Heat Measurement of Lithium-ion Battery

By

Zhong Zheng

A thesis submitted to the Graduate Faculty of
Auburn University
In partial fulfillment of the
Requirements for the Degree of
Master of Science

Auburn, Alabama
May 6, 2017

Keywords: Calorimeter, Heat generation, Kalman filter,
Thermal model, Thermal-electric module, Lithium-ion battery

Copyright 2016 by Zhong Zheng

Approved by

Song-Yul Choe, Chair, Professor of Mechanical Engineering
Roy Knight, Assistant Professor of Mechanical Engineering
Daniel Marghitu, Professor of Mechanical Engineering

Abstract

Since the temperature of the lithium-ion battery has a great impact on its performance and life, heat generation measurement of the lithium-ion battery becomes one of the most important parts of designing lithium-ion battery and battery management system (BMS). Commercial calorimeters are widely used in measuring heat generation rate of the lithium-ion battery but fail to measure large heat generation rate, and the response is slow. Therefore, this thesis presents a new calorimeter that consists of two thermal electric modules (TEMs) and two metal plates can measure large heat generation (120W) with a quick response (100s). A test station that constitutes with a bipolar power supply, an electronic load, and a DC power supply is built to test the designed calorimeter and the lithium-ion battery, it can charge/discharge the battery with any current profiles. All the equipments in the test station are controlled by LabVIEW. In order to identify the parameters of the metal plate and calibrate the calorimeter, a printed circuit board (PCB) is used as a dummy heat source. The PCB has the same size as the battery, and is assumed to have a pure electrical resistance. Therefore, the heat generation of the lithium-ion battery can be simulated. In order to control the temperature of the lithium-ion battery, different control methods are designed to control the current that is applied to the TEM. A lead-lag compensator has been selected by comparison because of its response time and stability. The calorimeter is thermally modeled based on the equation of energy balance of the metal plate. MATLAB/Simulink is used to simulate the calorimeter and the results are compared with the experimental data to validate the accuracy of the model. Based on the thermal model of the calorimeter, Kalman filter is used to estimate the heat generation rate of the lithium-ion battery. Finally, Kalman filter is implemented using MATLAB

and integrated into LabVIEW to measure heat generation rate of the lithium-ion battery in real time. The designed calorimeter is able to measure the heat generation of the lithium-ion battery accurately and fast.

Acknowledgement

I would like to express my deepest appreciation to my advisor, Dr. Song-Yul Choe, for giving me the opportunity to get involved in this research project. His wise suggestions and generous guidance assisted me to fulfill my Master study. With his valuable advice and detailed corrections to my papers and thesis, I could finish my research program successfully. I also would like to express thanks to my committee members, Dr. Roy Knight and Dr. Dan Marghitu, for their insightful instructions and comments, which enabled me to develop a deep understanding in the research area. Many thanks to my colleagues Yilin Yin, Xinchun Zhao, Yang Hu, Yalan Bi, Yinyin Zhao and Meng Xiao. They have helped me a lot on programming and experiments. Thanks to Vivien, she encourages me all the time. Last but not least, I would like to express my gratitude to my parents, Xiufeng Zheng and Guixia Wang, for their continuous support and encouragement.

Table of Contents

Abstract	ii
Acknowledgement	iv
Table of Contents	v
List of Tables	viii
List of Figures	ix
List of Abbreviations	xii
List of Symbols	xiv
Greek Symbols	xvi
1. Introduction	1
1.1. Background	1
1.2. Basics of lithium-ion battery	2
1.2.1. Fundamental chemical reactions in Li-ion battery	3
1.2.2. The effect of temperature on lithium-ion battery	5
1.3. Literature review	6
1.4. Motivations and Objectives	11
1.5. Thesis Outlines	13
2. Static calibration of the calorimeter	15

2.1. Test station setup.....	15
2.1.1. Test equipment	16
2.1.2. Test programming.....	17
2.2. Thermoelectric effect	17
2.2.1. Seebeck effect.....	18
2.2.2. Peltier effect.....	19
2.2.3. Thomson effect	21
2.3. Characteristics of Calorimeter.....	22
2.3.1. Governing equation of TEM.....	23
2.3.2. Structure of the Calorimeter	24
2.4. Modeling of the Calorimeter	26
2.4.1. Parameters identification of TEM	26
2.4.2. Identification of thermal parameters of the metal plate.....	34
2.4.3. Model Validation.....	38
3. Dynamic calibration of the calorimeter	42
3.1. Design of a temperature controller.....	42
3.1.1. Review of linear controllers	42
3.1.2. Selecting the controller.....	44

3.1.3. Implement of the lead-lag compensator	49
3.2. Design of the feed-forward element.....	50
3.3. Design of Kalman Filter.....	54
3.3.1. Basic of Kalman Filter.....	54
3.3.2. Implementation of Kalman Filter	56
3.4. Simulation	59
4. Heat generation measurement.....	67
4.1. Measurement of the PCB heat generation.....	67
4.2. Measurement of heat generation rate of lithium-ion pouch battery	70
4.2.1. Solid electrolyte interphase (SEI).....	70
4.2.2. Heat generation.....	72
4.2.3. Open circuit voltage (OCV) and SOC.....	75
4.3. Experiment	76
5. Conclusion and future work.....	83
5.1. Conclusion.....	83
5.2. Future work	83
References.....	85

List of Tables

Table 1: A comparison of different types of cells [1] [4]	2
Table 2: Typical Properties of different cathode active materials [1] [4].....	3
Table 3: Specifications of test equipment.....	16
Table 4. Characteristics of Aluminum.....	29
Table 5: Parameters identification of TEM	33
Table 6 The initial values of the solution for equation (2-18)	35
Table 7: Data used for determining K.....	37
Table 8: Effect of the parameters.....	43

List of Figures

Figure 1: Structure of a Li-ion battery [3]	4
Figure 2: Configuration of the calorimeter [14]	10
Figure 3: Comparison between measured and estimated heat generation rate [14]	10
Figure 4: Test station wiring diagram.....	15
Figure 5: Test station photograph	16
Figure 6: Schematic diagram of Seebeck effect	19
Figure 7: Schematic diagram of Peltier effect	20
Figure 8: Schematic diagram of Thomson effect.....	21
Figure 9: Working mechanism of TEM.....	22
Figure 10: A P-N junction energy flow scheme	23
Figure 11: Structure of part the calorimeter.....	25
Figure 12: Control volumes of the metal plate	27
Figure 13: Determine the characteristic time.....	29
Figure 14: Temperature profile of metal plate in PCB side.....	32
Figure 15: Comparison of experimental values and estimated value	34
Figure 16: Comparison between experimental data and equation (2-19).....	36
Figure 17: Model validation.....	39
Figure 18: Expanded view of the transient behaviors.....	40
Figure 19: A screenshot of parameter tuner.....	45
Figure 20: Block diagram for controller and TEM.....	46

Figure 21: Step response of the system with different controllers.....	47
Figure 22 The Bode plot of the lead compensator	48
Figure 23: The Bode plot of the lead-lag compensator.....	49
Figure 24: The response of the system when different disturbance applied.....	51
Figure 25: Block diagram of a system with feed-forward element	51
Figure 26: Comparison between the outputs of controller with/without FF element	53
Figure 27:Block diagram of observer	55
Figure 28: The block diagram of the calorimeter system	59
Figure 29: Comparison between the fitting curve and experiment data	60
Figure 30: Block diagram of the calorimeter	62
Figure 31: Temperature of the metal plate in PCB side.....	63
Figure 32: (a) The current applied to the calorimeter (b) Estimated heat generation rate of the calorimeter	64
Figure 33: (a) Comparison between the estimation result and the simulation result (b) Zoomed-in dynamic response.....	65
Figure 34: Estimated results by Kalman filter	66
Figure 35: Current applied to the calorimeter.....	68
Figure 36: Comparison between the calculated and real heat generation rate.....	68
Figure 37: Static performance of Kalman filter estimation	69
Figure 38: Dynamic performance of Kalman filter estimation.....	69
Figure 39: An initial cycle in charge model.....	71

Figure 40: An initial cycle in discharge model.....	72
Figure 41: SOC-OCV curve.....	76
Figure 42: Temperature of the clamp.....	77
Figure 43: Heat generation of the battery during discharge	78
Figure 44: Performance of the calorimeter at discharging.....	79
Figure 45: Heat generation of the battery during charge	80
Figure 46: Performance of the calorimeter at charging	81

List of Abbreviations

ARC	Accelerated-rate Calorimeter
BIL	Battery-in-the-loop
BMS	Battery Management System
CC	Constant Current
CT	Current Transducer
CV	Constant Voltage
DAQ	Data Acquisition
DC	Direct Current
EMF	Electromotive Force
EV	Electric Vehicle
FF	Feed-Forward
GM	Gain Margin
HDPE	High-density Polyethylene
HEV	Hybrid Electric Vehicle
IHC	Isothermal Heat Conduction Calorimeter
KF	Kalman Filter
OCV	Open Circuit Voltage
P	Poles

PCB	Print Circuit Board
PID	Proportional, Integral and Derivative Controller
PLC	Programmable Logic Controller
PM	Phase Margin
PV	Processing Variable
RV	Reference Value
SEI	Solid Electrolyte Interphase
SOC	State of Charge
TEM	Thermoelectric Module
VCR	Vapor-compression Refrigeration
Z	Zeros

List of Symbols

A	Surface area (m^2) or state matrix
B	Input matrix
C	Output matrix
c	Concentration ($\text{mol}\cdot\text{L}^{-1}$)
C_p	Heat capacity ($\text{J}\cdot\text{kg}^{-1}\cdot\text{K}^{-1}$)
D	Disturbance of the system
E	Potential difference (V)
e_{ss}	Steady State Error
F	Faraday's constant ($96,487 \text{ Coulombs}\cdot\text{mol}^{-1}$)
G	Gibbs free energy (kJ)
h	Heat transfer coefficient ($\text{W}\cdot\text{m}^{-2}\cdot\text{K}^{-1}$)
H	Enthalpy (kJ)
I	Current (A)
K	Thermal conductivity ($\text{W}\cdot(\text{K}\cdot\text{m})^{-1}$) or controller gain
L	Observer gain
m	Mass (kg)
M_p	Overshoot
P	Power (W)

q'''	Volumetric heat source ($\text{W}\cdot\text{m}^{-3}$)
Q	Heat generation/pump rate (W) or Capacity (Ah)
R	Resistance (Ω)
S	Entropy (kJ)
t	Time (s)
T	Temperature ($^{\circ}\text{C}$ or K)
u	Input
U	Chemical potential (V)
V	Voltage (V) or Volume (m^3)

Greek Symbols

α	Seebeck coefficient ($V \cdot K^{-1}$)
γ	ARC constant ($W \cdot K^{-1}$)
κ	Ionic Conductivity of electrolyte ($S \cdot cm^{-1}$)
κ_D	Diffusion conductivity ($A \cdot cm^{-1}$)
ρ	Density ($kg \cdot m^{-3}$)
Π	Peltier coefficient (V)
σ	Conductivity of solid active material ($S \cdot cm^{-1}$)
τ	Thomson coefficient ($V \cdot m \cdot K$)
ϕ	Potential in a phase (V)

1. Introduction

1.1. Background

In recent decades, people pay more concern on the environmental pollution, and the emission is becoming more and more stringent. Automobile companies, on the one hand, try to improve the efficiency of the traditional internal combustion engine; on the other hand, put much effort to develop hybrid electric vehicle (HEV) and electric vehicle (EV). With a great improvement in battery technologies, the average unit price of the lithium-ion battery is reduced by 50% in twenty years [1]. Therefore, HEVs and EVs become more important in automobile industry. In order to better protect the lithium-ion battery (including control its environment, balancing cells, etc), battery management system (BMS) need further development. Temperature is an important state of the lithium-ion battery that BMS should monitor because both high temperature and low temperature have a great impact on the lithium-ion battery's performance and life. Therefore, measurement and estimation heat generation rate of the battery play an critical role in designing of the lithium-ion battery and BMS.

Some researchers use the commercial calorimeters to measure the heat generation rate of the battery [2]. However, most of the calorimeters in the market are very expensive and have large sizes, measurement range is not enough for the high power battery as well. Moreover, the commercial calorimeters have a slow response due to a relatively large thermal time constant. Therefore, a new calorimeter was designed which consists of two thermal electric modules (TEMs) that allow measuring the large heat generation rate. A lead-lag compensator was used to control the surface temperature of the metal plate and the battery. A thermal model of the designed calorimeter was built; then Kalman filter was applied to make calorimeter respond rapidly and accurately.

1.2. Basics of lithium-ion battery

Lithium-ion battery is widely used in industry because of its high power, high energy density, and lower cost. Based on the way of packaging, the lithium-ion battery can be manufactured into four different types: button, pouch, cylindrical and prismatic [3]. The advantages and the disadvantages of these types of the batteries are summarized in Table 1. According to the materials used in the cathode, the lithium-ion battery can be classified as LiCoO_2 , LiMn_2O_4 , LiFePO_4 , etc. [3]. Some typical properties of the commercial lithium-ion battery are summarized in Table 2.

Charge or discharge rates are usually denoted as C-rates (A). C-rate is determined by the capacity of the battery. For example, a battery's capacity is 15.6 Ah. When the battery is discharged from 100% state of charge (SOC) to 0% SOC, the current corresponding to 1C is 15.6A, and it takes an hour to fully discharge the battery. 2C means discharging the battery with 31.2A DC, and it only takes half an hour to complete discharging.

Table 1: A comparison of different types of cells [1] [4]

Construction	Advantages	Disadvantages
Cylindrical	High specific energy Good mechanical stability Long calendar life and low cost	Less packaging density
Button	Low cost Space-efficient	No safety vent Long charge time
Prismatic	Space-efficient	High cost Sensitive to humidity and temperature

Pouch	Light and cost-efficient Space-efficient	Sensitive to humidity and temperature
-------	---	---------------------------------------

Table 2: Typical Properties of different cathode active materials [1] [4].

Characteristic	LCO	LMO	LFP
Positive Electrode	LiCoO ₂	LiMnO ₄	LiFeO ₄
Negative Electrode	Graphite	Graphite	Graphite
Nominal Voltage (V)	3.6-3.7	3.7-3.8	3.2-3.3
Operating Voltage (V)	2.5-4.2	2.5-4.2	2.5-3.6
Specific Energy (Wh/kg)	175-200	100-240	60-110
Energy Density (Wh/L)	400-640	250-640	125-250
Cycle Life(100% to 80% capacity)	500+	500+	1000+
Commercially Available	1991	1996	1996

1.2.1. Fundamental chemical reactions in Li-ion battery

The lithium-ion battery consists of four main components: anode, cathode, electrolyte, and separator. The voltage and the capacity of a lithium-ion battery are determined by the material of the electrodes. The major cathode materials are lithium compounds, and anode used in lithium ion battery are graphite. In general, the electrolyte material of lithium-ion battery is polymer, because the polymer is a good medium that can transport Li-ion, whereas it cannot carry electrons. Moreover, polymer is also a good insulator to prevent shorting inside of the battery. The structure of a Li-ion battery is shown in Figure 1.

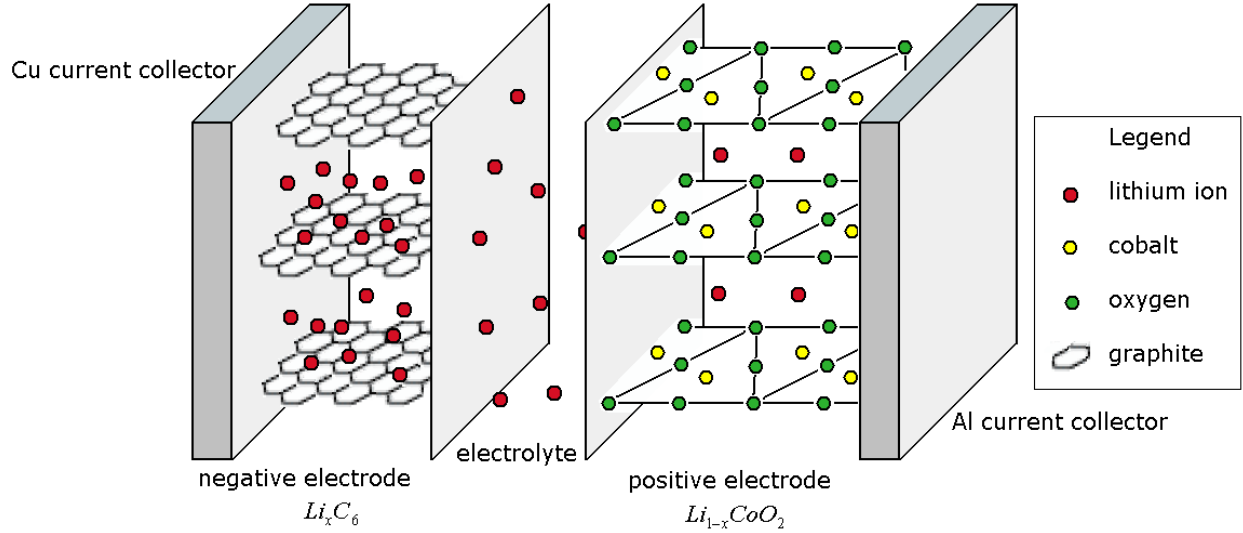
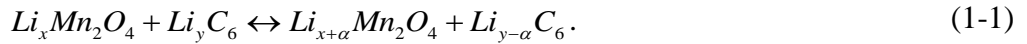


Figure 1: Structure of a Li-ion battery [3]

The battery that used in this study is LiMn₂O₄/Carbon pouch cell. The battery's capacity is 15.7Ah; operating voltage is between 2.5V and 4.15V; the dimension of the active material is about 20cm×15cm×0.5cm. There are plenty of chemical reactions in this kind of battery. Tom Eriksson made a full discussion about the chemical reactions inside of the battery [5]. The major reaction is:



During discharging, the Li-ions go through the separator from the anode to the cathode, with electrons flowing through the circuit. Therefore, a reduction reaction takes place at the cathode, while an oxidation reaction takes place at the anode, and vice versa during charging. In thermodynamics, the change in energy is a function of changes in Gibbs free energy in Li concentration. The Gibbs free energy (G) is defined as:

$$G = H - TS, \quad (1-2)$$

where H is enthalpy, T is absolute temperature and S is entropy. Then the chemical potential (μ) is defined as:

$$u = \frac{\partial G}{\partial x}, \quad (1-3)$$

where x is the number of inserted Li atoms.

Moreover, the change of the free energy can be presented as:

$$\Delta G = -nF\Delta E, \quad (1-4)$$

where n is the number of electrons, F is Faraday's constant, E is the potential difference between cathode and anode, α is in equation (1-1). Combining (1-3) and (1-4), the relationship between electrical energy and chemical energy of the battery is defined as:

$$-nF\Delta E = u_c - u_a, \quad (1-5)$$

where u_c and u_a are the chemical potentials of the lithium ions in cathode and anode, respectively.

1.2.2. The effect of temperature on lithium-ion battery

When the battery is charging or discharging, a large amount of heat could be generated due to Joule heating and oxidation processes. These phenomena have a great impact on the performance of the battery. When a battery is working under an elevated temperature, it will accelerate decomposition of the binder and electrolyte, ultimately causing the capacity fade. At the same time, the elevated temperature accelerates the chemical reaction between the electrolyte and the electrode, the by-product can decrease the surface area of active material that blocks lithium-ion transport from the electrolyte to the electrode, eventually leading to the power fade [6]. Also, due to the loss of active material, the power degradation is significantly enhanced at elevated temperature [7]. Gerardine G. Botte indicated that temperature could also affect other important parameters of the battery, such as the conductivities and the diffusion coefficients [8]. Shriram Santhanagopalan and his group member cycled their battery 200 times at different temperature. It

shows that under elevated operating temperature (308.15K and 318.15K compared to 298.15K), the capacity fades by 66.10% at 308.15k and by 87.46% at 318.15K, which is drastically higher than 25.93% at 298.15K [7]. Therefore, battery manufacturers attribute great importance to the high thermal stability and active material degradation [9].

On the one hand, the elevated temperature can lead to capacity fade and power fade of the battery. On the other hand, the low temperature can severely shorten the cycle life of the battery due to the lithium-ion being not able to diffuse into the graphite [10]. Moreover, the low-temperature increases resistance of the anode when the battery is charging, which leading to the power fade [11]. Researchers from Tsinghua University tested LiFePO₄ battery at 263.15K and reported that over 85% capacity fades after 50 cycles [11]. The capacity fade is even more severe under the low temperature than at elevated practical temperature.

In order to minimize the temperature effects on the lithium-ion battery, either heat at a low operating temperature or heat pump at a high operating temperature should be generated. In reality, the battery modules or packs consist several cells and myriads of heat is generated during charging and discharging- therefore, an active cooling strategy is always required [12]. Facing the low-temperature issues, a new charging model was applied to the LiFePO₄ battery: current pulses can heat the battery to avoid the low-temperature effect during charging [13].

In summary, the temperature affects the performance and the degradation of the lithium-ion battery significantly. Therefore, estimation and accurately measurement of heat generation play a pivotal role not only in BMS but also in designing and safety of the lithium-ion battery.

1.3. Literature review

Heat generation rate of the lithium-ion battery can be measured directly by commercial calorimeters. There are two kinds of calorimeters are widely used: accelerated-rate calorimeter

(ARC) and isothermal heat conduction calorimetry (IHC) [14]. In general, the ARC method measures the heat generation rate of the lithium-ion battery based on the increase of the battery's temperature and the total heat exchange from the battery to surroundings. It can be described by the energy balance equation under the natural convective heating condition. The governing equation is:

$$C_p m \frac{dT}{dt} = Q - hA(T - T_a). \quad (1-6)$$

The boundary condition is: $T=T_i$ at $t=0$. T_a is the ambient temperature. Where C_p is the heat capacity of the cell ($J\ kg^{-1}\ K^{-1}$); m is the mass of the cell (kg); T is the temperature of the cell (K); T_a is ambient temperature (K); Q is the heat generation rate of the cell (W); h is the effective heat transfer coefficient ($W\ m^{-2}\ K^{-1}$); A is the surface area of the cell (m^2). The product of effective heat transfer coefficient and the surface area (hA) is also called ARC constant γ ($W\ K^{-1}$). When heat source term is 0, the solution of equation (1-6) is

$$\ln\left(\frac{T - T_a}{T - T_i}\right) = \frac{hA}{C_p m} t.$$

Heat capacity, mass and surface area of the cell are known, ambient temperature and cell temperature are measured directly. Then calculate h based on equation (1-6). So far, all the parameters are known, and instantaneous heat dissipation rate from the cell to the surroundings can be defined as:

$$Q_{dissipation} = \gamma(T - T_a).$$

(1-7)

Once the instantaneous heat dissipation rate is determined, the heat generation rate of the cell is determined by equation (1-6).

On the other hand, the IHC method measures the heat generation rate of the lithium-ion battery based on the instantaneous thermal power which is measured by a heat flow sensor located between the battery and a heat sink. The total heat can be calculated by integrating the thermal power with time.

Hong and his team used an ARC (ARC2000, Columbia Scientific Industries) to measure the heat generation rate of a cylindrical lithium-ion battery with a capacity of 1.35Ah. They discharged the battery with 1C, 0.33C, and 0.5C at different temperatures [15]. However, the measured heat generation rate was usually under 1W. Using the same method, Al Hallaj measured the heat generation rate of an 18650 lithium-ion battery; the discharge rate was less than 0.1C and the maximum heat generation rate he found was only 0.26W [16]. Kim, Prakash, and Selman used an isothermal microcalorimeter to measure the heat generation rate of a LiMn_2O_4 coin-type cell. They kept their heat sink temperature at 298.15K, and used thermoelectric sensors that was located between the test cell and the heat sink to detect the heat produced by the cell [17]. All their tested batteries were the low power batteries that applied to portable appliances, and the calorimeters were limited by low maximum measurement power.

Forgeza developed a simplified thermal model that can determine the heat transfer coefficients and the heat capacity of the battery by experiments [18]. He used two thermal couples; one was introduced into a cylindrical lithium-ion battery's positive electrode side, and the other one was placed on the surface of the battery. According to the equation of energy balance, he assumed that the heat flux generated inside of the battery (Q_n) through the battery was the same as the heat flux that from the surface of the battery to the environment. Therefore, the heat flux conservation equation came out to be:

$$Q_n = h_{in}A(T_{in} - T_{surf}) = -h_{out}A(T_{amb} - T_{surf}). \quad (1-8)$$

Then the heat transfer coefficient and the heat capacity of the battery can be determined by steady state and transient part, respectively.

His work predicted the inner temperature of the battery that was pivotal to BMS and simple enough to be implemented. In addition, the heat transfer coefficient and the heat capacity of the lithium-ion battery are two key parameters to make a precise measurement of the heat generation rate. However, this method cannot be applied to our test because it is impossible to drill a hole in a pouch cell. The battery we are tested has high power and capacity. The internal structure of the battery is complicated, therefore, it cannot be guaranteed with that putting a thermal-couple into the battery will not make the battery leak, even with careful handling. It is very likely to make a short circuit inside of the battery or even cause an explosion.

Kaiwei Chen designed a special calorimeter to measure heat generation of the prismatic battery that was quite similar to our batteries not only in battery size but also in capacity. They assumed that the total heat generated by the battery was conducted through a high-density polyethylene (HDPE) slab into a constant temperature heat sink. Based on the convolution theorem:

$$\Delta T_m = \int_{t_0}^t Q_{battery}(\tau)\Phi(t-\tau)d(\tau),$$

and according to the measured temperature change, heat generation rate of the Li-ion battery can be obtained [14]. Where ΔT_m is the overall temperature change of the calorimeter, $Q_{battery}(\tau)$ is heat generation rate of the battery, $\Phi(t-\tau)$ is the apparatus function. The following is a part of his calorimeter scheme.

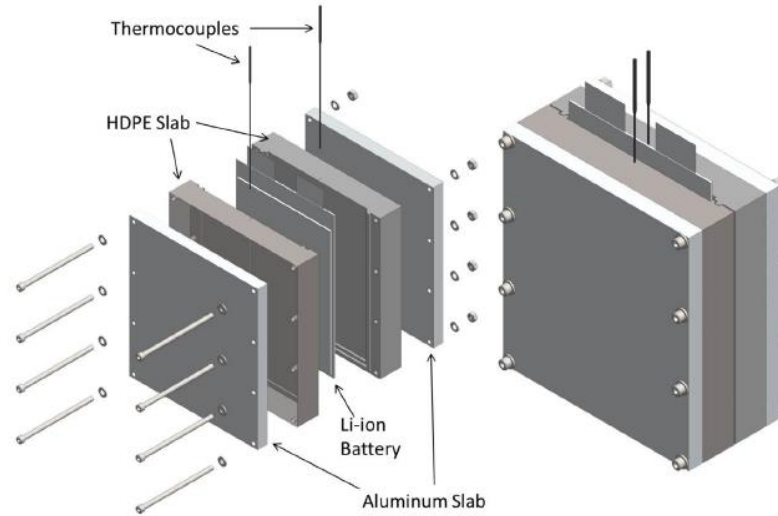


Figure 2: Configuration of the calorimeter [14]

However, the HDPE slab he chose was five times the thickness of the battery. Therefore, a limited heat transfer capability leading a long time constant of his calorimeter, and his calorimeter cannot meet the transient behavior of the battery's heat generation rate. The following figure shows that the calorimeter needs about 1 hour to follow up a step heat generation. Heat generation rate of the battery could be changed during charging and discharging in our testing. Therefore, a long time constant is not able to provide an accurate measurement of the transient heat generation rate.

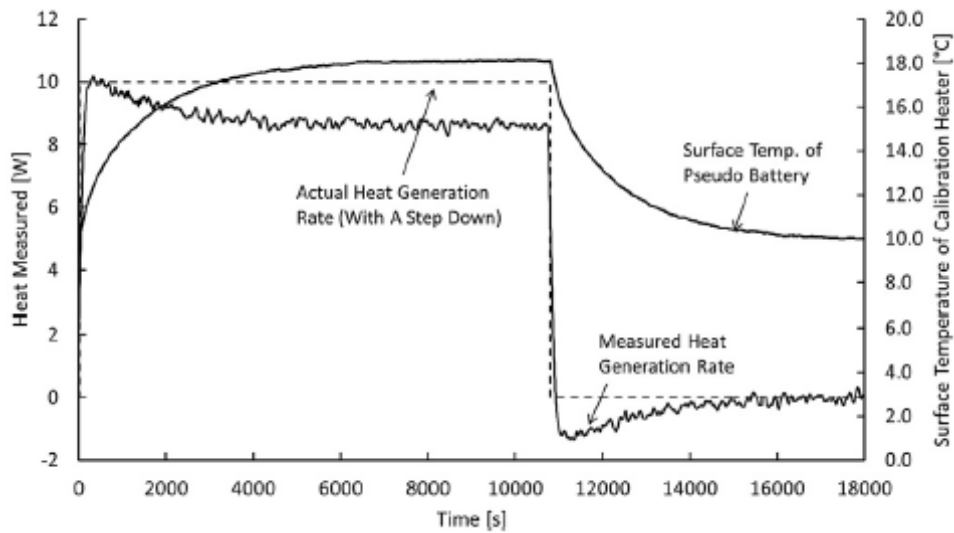


Figure 3: Comparison between measured and estimated heat generation rate [14]

1.4. Motivations and Objectives

The main objective of BMS is to protect the battery. Therefore, a BMS should prevent the battery from over-current, under-current, over-voltage, under-voltage, over-temperature, under-temperature. However, these functions are far away from optimizing states of the battery and slowing down the aging process of the battery. It is worth of mentioning that the current and voltage are usually dependent on how much power the battery could provide. The temperature of the battery is relatively simple to control and optimize. Like mentioned earlier; temperature has a great impact to the lithium-ion battery. Therefore, controlling the temperature can be one of the most efficient ways to slow down the aging process of the battery.

The temperature of the battery varies when the battery is charged and discharged due to the internal heat generation [19]. In order to control the temperature of the battery, it is important to estimate and measure heat generation rate of the battery. However, the accurate heat generation rate estimation is very complicated due to reversible heat generated by the change of entropy, and irreversible heat generated by Joule heating, charge-transfer overpotentials and mass transfer limitations [20]. The reversible heat and the irreversible heat are also effect by changing electrode resistivity due to current density, the complex behavior of the interfacial areas of the electrode and electrolyte, and etc. Not only these conditions need to be considered, but also the mentioned parameters are temperature dependent. Therefore, an electrochemical model needs further development to make estimation of the heat generation rate more precise [21]. However, electrochemical model is not presented in this study, this study focus on measuring heat generation rate of the lithium-ion battery directly.

After reviewing the above literature, the previous works on measuring heat generation rate have the following limitations: First, cylindrical or coin type cells that are in small size, capacity,

and low power were tested by most of them. These kinds of batteries are not suitable for HEVs or EVs that need a high power and large capacity battery. Second, all of them can only measure a relatively small heat generation rate of the magnitude is from 0.1 W to 20W. In this study, a large current will be applied to the battery to meet the fast charging requirement. Heat generation rate's range is usually between 20W and 110W, so that the commercial calorimeter are not used. Third, most of them did not show any details of their response time to a step signal. Some of them showed the response time, but it took more than 3,000 seconds to follow up a step signal that fail to meet our requirement of transient behavior.

Therefore, the objective of the present study is to measure a large heat generation rate of the battery that applicable for HEVs and EVs, as well as to measure a quick heat generation rate.

1.5. Thesis Outlines

The full configuration of my thesis is as follows:

1. Introduction

First, this chapter elaborates the background of this research. Second, it briefly introduces the basics knowledge of the lithium-ion battery and temperature impact on the lithium-ion battery in more details. Third, it shows a plenty of work that other researchers have conducted, including their methods and results. Finally, the motivation and objective of this study are addressed.

2. Parameter Identification

First of all, this chapter elaborates on the test station we designed. Then the characteristics of the designed calorimeter's core part are introduced: thermal electric module (TEM). Five effects are introduced that are integral in the TEM and 11 sets of experiments have done to determine the parameters of the TEMs. A thermal model of the metal plate is built, the heat capacity and the heat conductivity are calculated in theory and identified by using the least square method. A comparison between the simulation and experimental data are shown that the model and the identified parameters are close to the true values.

3. Dynamic calibration

First, we select a lead-lag compensator to be the controller for maintaining the temperature due to its stability and quick response. Then a feed-forward element is applied to the system to optimize the overshoot. Kalman filter is introduced and applied to estimate the states of the designed calorimeter. Finally, a simulation based on 'SIMULINK' simulates the whole process of the test station and compares with the estimation of Kalman filter.

4. Heat generation rate measurement of the PCB and the lithium-ion battery

First, the calorimeter is used to measure heat generation rate of a PCB, because we can control its heat generation rate as a constant, and then compare the heat generation rate measured by the designed calorimeter with the real generation rate of the PCB. This work aims to test the performance of the calorimeter. Second, the calorimeter measures the heat generation rate of the battery under different charge and discharge rate, and then compares the results between the experimental data and theory calculation.

5. Conclusion and future research

Summarize the results of this study and discuss the remaining works that can improve the performance of the calorimeter.

2. Static calibration of the calorimeter

2.1. Test station setup

A battery test station is designed and constructed so that it can charge and discharge the lithium-ion battery with any desired current profile. The terminal voltage, charge/discharge current, and temperature of the lithium-ion battery can be measured directly and be recorded by the data acquisition (DAQ) board. SOC and heat generation rate of the lithium-ion battery can be estimated based on the above profiles. The battery test station has a programmable logic controller (PLC) (Not show in figure 4 and figure 5) which is used to protect the battery from over-charging and over-discharging. The PLC works independently and can measure the battery terminal voltage directly. Once the terminal voltage of the battery is higher/lower than the maximum/minimum limit voltage of the battery, PLC will cut off the charge/discharge loop immediately. An overall test station wiring diagram is shown in Figure 4, and a picture of the test station is shown in Figure 5.

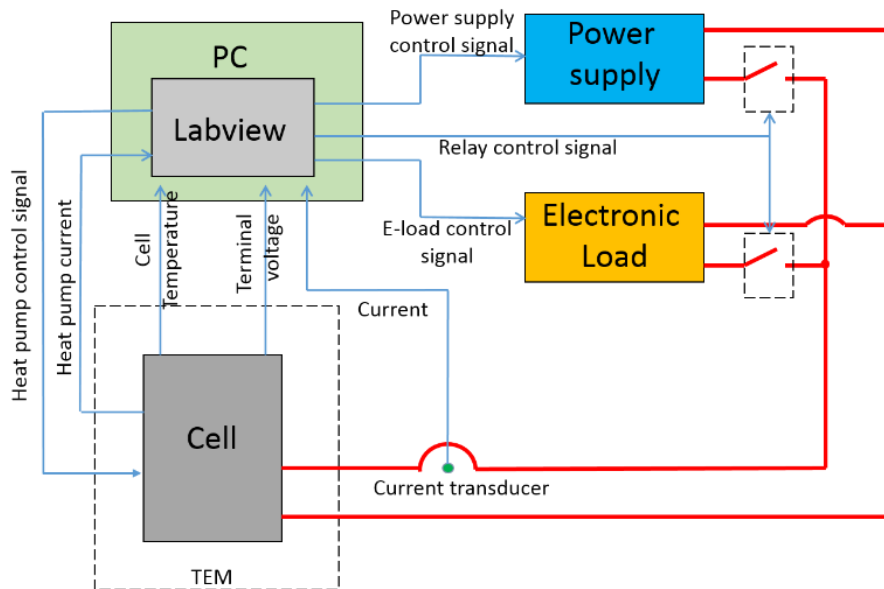


Figure 4: Test station wiring diagram

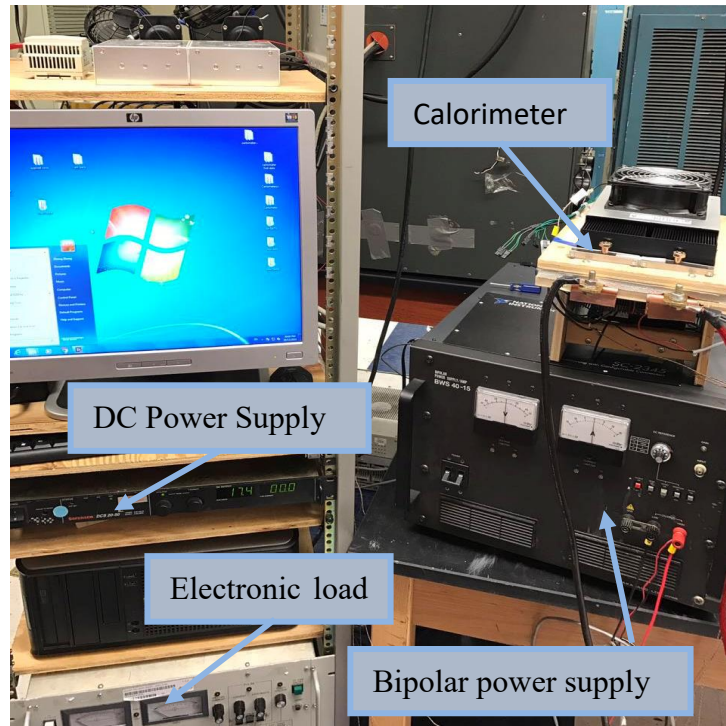


Figure 5: Test station photograph

2.1.1. Test equipment

A DC power supply is used to charge the battery, and an E-load is used to discharge the battery. A bipolar power supply is used to provide the power needed for the TEMs. The list of the test equipment is shown in Table 3.

Table 3: Specifications of test equipment

Equipment	Specification	Value
Power supply	Maximum current	125A
E-load	Maximum current	300A
Bi-polar power supply	Operating Current	-15A~15A
TEM	Operating current	-7.4A~7.4A
Voltage Sensor	Measurement range	0-50V
Current Sensor	Measurement range	0-200A

Thermocouple	Measurement range	-190°C~260 °C
Data acquisition	Channel	16 Analog inputs 2 Analog outputs 24 Digital inputs/outputs

The inputs/outputs of the National Instruments (NI) connector block and modules are voltage signal, which allows a user to use analog or digital inputs/outputs. Analog inputs/outputs are used to control the bipolar, E-load, and DC power supply. Digital inputs/outputs are used to control the relays in the battery test station. A calibration is needed before testing. Taking current calibration as an example: The current sensor used in the test station is a current transducer (CT). The CT transforms the current signal which passing through it into a much smaller current at a ratio of 2000:1 theoretically. Then a 10Ω precision resistor with a tolerance of 0.01% is series with the CT. The voltage across the precision resistor as an input signal goes to the module. The CT is calibrated through the use of a current probe and associated error less than 0.2%.

2.1.2. Test programming

The test station is designed to facilitate the integration of controls written by MATLAB and LabVIEW code, which is called battery-in-the-loop (BIL). Any algorithms written using MATLAB code can be embedded. Therefore, some variables that cannot be measured directly can be obtained by estimation. For example, the Coulomb’s method is embedded to estimate SOC, while Kalman Filter is embedded to estimate heat generation rate of the battery.

2.2. Thermoelectric effect

The thermoelectric effect describes the conversion between temperature difference and electric voltage. A thermoelectric device creates a temperature difference when there is a voltage

applied to it and vice versa. Based on this characteristic, the thermoelectric effect can be used to measure temperature or generate electricity, for instance, thermocouple, solid cooler and heater. The critical parts of the calorimeter are two TEMs which are thermoelectric devices. There is three separately identified thermoelectric effects domain on the TEM: Seebeck effect, Peltier effect, and Thomson effect.

2.2.1. Seebeck effect

When two different materials and different temperature of metal A and B are connected into a loop, the closed loop will generate a current, which the phenomenon is called Seebeck effect. As shown in figure 7, the temperature at joints 0 and 1 are T_h and T_c ($T_h > T_c$), respectively. Then the open circuit will produce an electromotive force, known as the Seebeck electromotive force (EMF). The value is :

$$\Delta V_{CD} = \alpha_{AB}(T_h - T_c) .$$

When the temperature difference is not great, it can be considered that α_{AB} is constant and the constant is called Seebeck coefficient. It can be defined as :

$$\alpha_{AB} = \frac{dV_{CD}}{dT} .$$

The unit of the Seebeck coefficient is V/K. From the above equation, we can see that Seebeck coefficient can be positive or negative determined by the polarity of the voltage that applied to the metal.

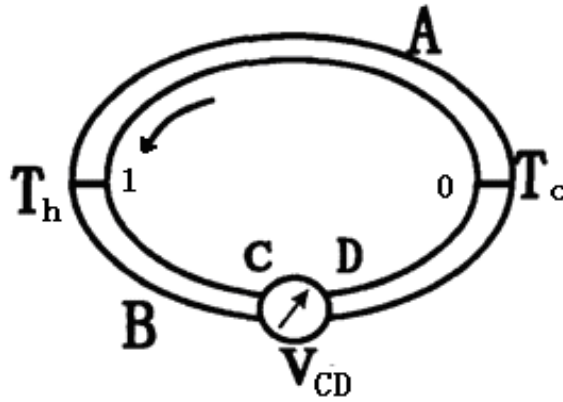


Figure 6: Schematic diagram of Seebeck effect

At the atomic scale, a temperature gradient can cause the unevenly charge carriers distribution in the material. Taking a metal bar, for example, assumed that the electrons in the metal bar is gas. According to the molecular motion theory, when a temperature difference applied on two sides of the bar, the average kinetic energy of hot side of the metal bar is larger than that of the cold side of the metal. Therefore, the speed of electrons on the cold side is slower than the hot side's electrons, then from the overall view, the electrons go to the cold side of the metal bar from the hot side. Due to the uneven distribution of the electrons, there is an electromotive force generated inside of the metal bar and finally, enters an equilibrium state.

2.2.2. Peltier effect

When the current flows within a closed loop that is constructed by two different types of conductors, there will be the heat generation and the heat absorption at the electrified junctions, respectively. As is shown in Figure 7: Schematic diagram of Peltier effect, this phenomenon is called Peltier effect and the heat generated and absorbed called Peltier heat.

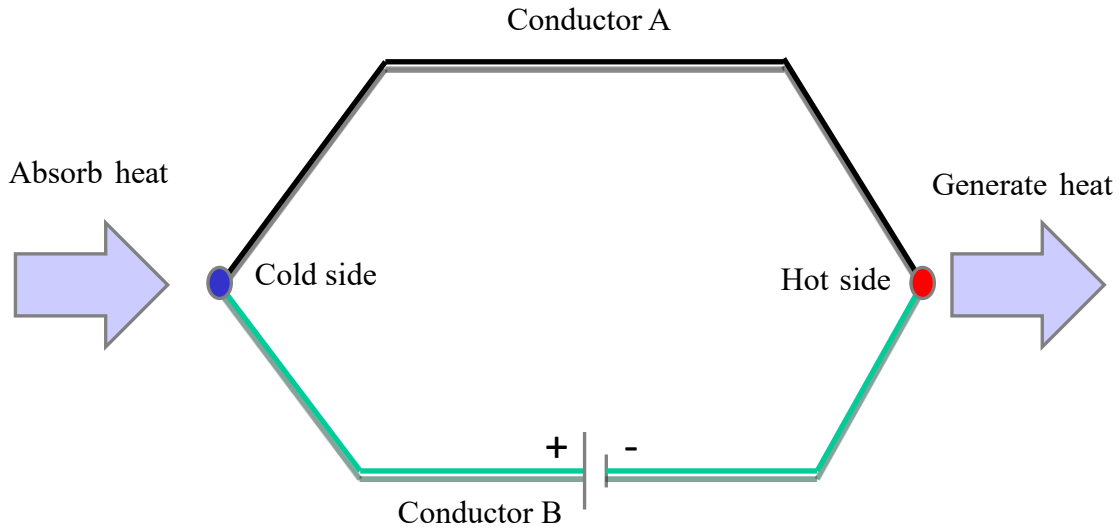


Figure 7: Schematic diagram of Peltier effect

The heat generation or absorption (Q) at the junctions is proportional to the current (I) that flows within the circuit. The relationship is as following:

$$Q = \Pi \cdot I, \quad \Pi = \Pi_A - \Pi_B, \quad \Pi = (\alpha_A - \alpha_B) \cdot T,$$

where Π is the Peltier coefficient, Π_A and Π_B is the Peltier coefficient of conductor A and B, respectively. T is the absolute temperature of the junction.

From the above equation, the cool side or the hot side can be swapped due to the change of the current direction. Peltier effect is the key characteristic that makes the thermoelectric device to behave as a cooler or heater.

At the atomic scale, the Peltier coefficient can be considered as the unit charge's ability of carrying heat. When the current flows in a circuit, charges continuously travel through the junction. Different materials have different Peltier coefficients, in other words, different abilities of carrying heat. Therefore, when traveling through the junction, the charge's ability of carrying heat becomes weaker, the junction will release heat, if the ability of carrying heat becomes stronger, the junction will gain heat from the environment.

2.2.3. Thomson effect

The Seebeck coefficient of a conductor is different under different temperatures. Therefore, a spatial gradient in temperature causes a gradient of the Seebeck coefficient. When the current flows through this gradient, the heat generation or the heat absorption can be observed. This phenomenon is called Thomson effect, as described in the following equation:

$$dQ_{Th} = -\tau \cdot I \cdot \frac{dT}{dx},$$

where dQ_{Th} is heat generation/absorption rate, τ is the Thomson coefficient, I is the current flows in the conductor, and dT/dx is the temperature gradient. Thomson effect scheme is shown in Figure 8.

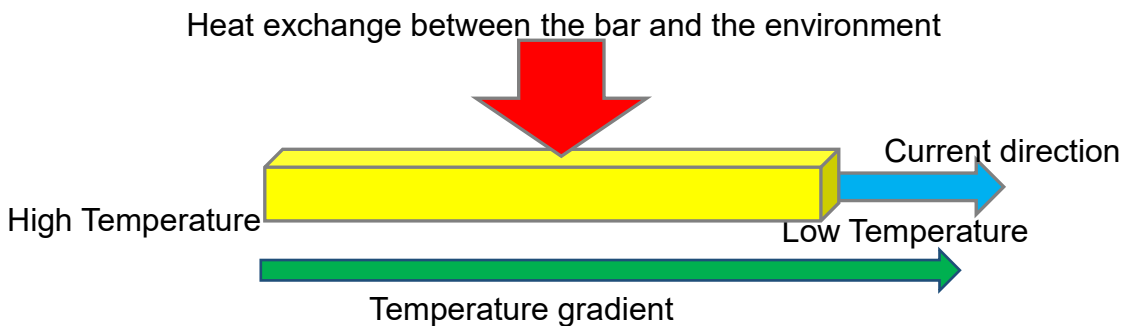


Figure 8: Schematic diagram of Thomson effect

2.3. Characteristics of Calorimeter

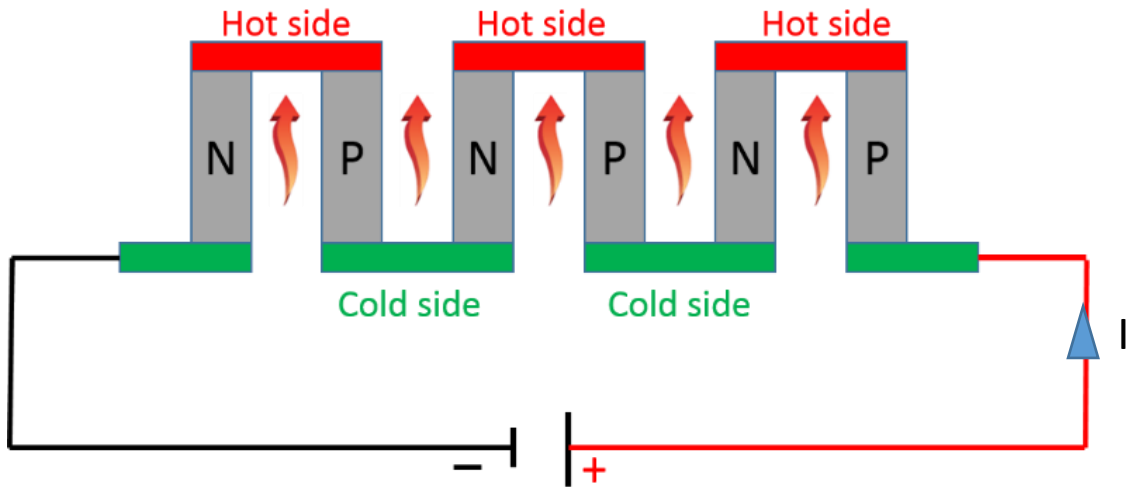


Figure 9: Working mechanism of TEM

Thermoelectric module (TEM) is the core part of the designed calorimeter. It's not as common as vapor-compression refrigeration (VCR), because comparing to the VCR, the efficiency is lower than VCR's. However, the TEM has a longer life and never leaks. Having less components and no circulating liquid, the TEM has a relative small size and flexible shapes which fits better for laboratory applications. Based on the working mechanism, the TEM has a hot and a cold side during its working period. A schematic diagram is shown in Figure 9: Working mechanism of TEM.

The key components in the TEM are the semiconductors (P-N junction) that is placed thermally in parallel and electrically in series to each other. When a voltage is applied to the P-N junctions, the electrons in the N-type junction and the holes in the P-type junction move from the cold side to the hot side. With the electrons and holes flowing through the P and N-type junction, heat is absorbed in the bottom and is transported to the top due to the Peltier effect. Therefore, one side becomes cooler and cooler, and the other side becomes hotter and hotter. The cold and hot side of the TEM is determined by the direction of the current.

2.3.1. Governing equation of TEM

Seebeck effect, Peltier effect, and Thomson effect are reversible effects in the TEM; there are also two effects that are irreversible in the TEM: Fourier effect and Joule effect. The heat generation by Thomson effect is very difficult to measure and not significant compared to Joule effect. Therefore, this study ignores the Thomson effect.

Figure 10 shows the energy flow in a P-N junction, the bottom is the hot side, and the top

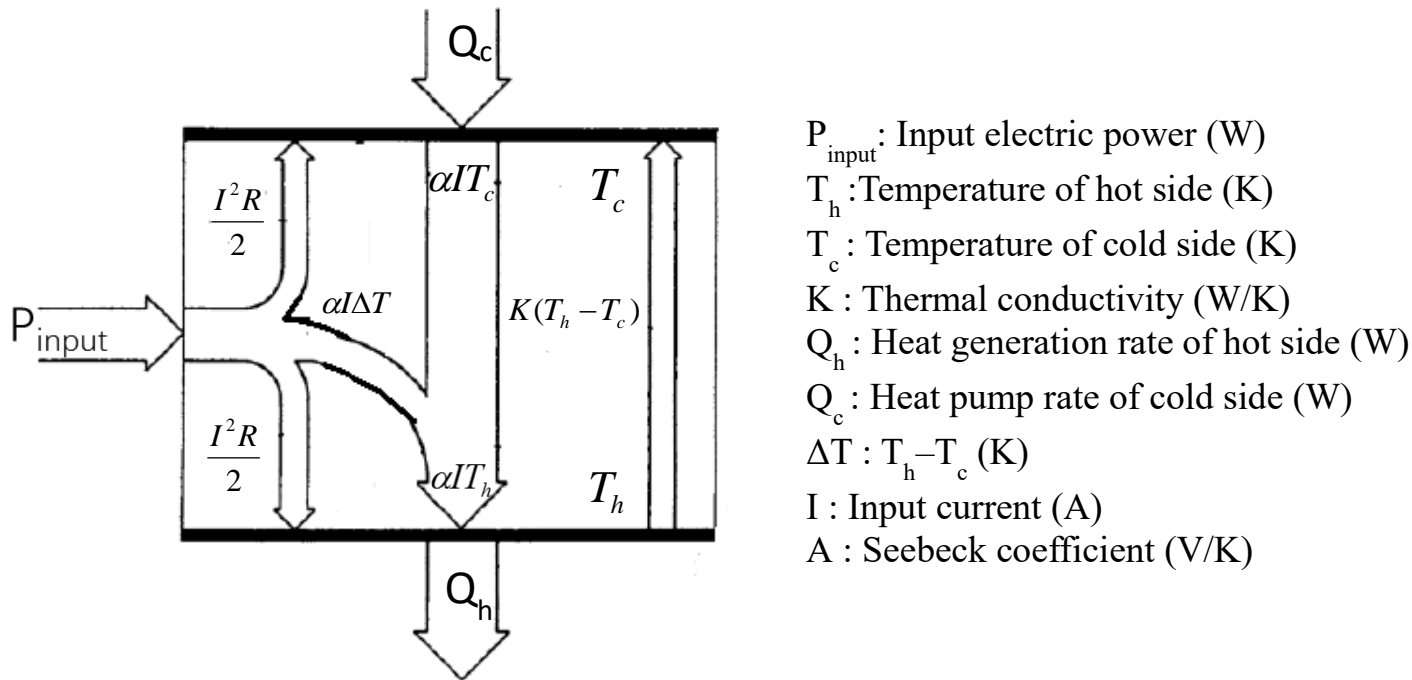


Figure 10: A P-N junction energy flow scheme

is cold side. When an input power goes into a P-N junction, it can be divided into two parts, the first one is Joule heating due to the resistance of the P-N junction, which is generated inside of the P-N junction. It is assumed that half of it goes to the cold side, the other half goes to the hot side. The second part is the heat transfer from the cold side to hot cold side due to Peltier effect. The input power can be described as:

$$P_{input} = I^2R + \alpha I \Delta T = IU , \quad (2-1)$$

where U is the voltage across the P-N junction. Equation 2-1 describes the input power required to overcome the Seebeck effect ($\alpha I \Delta T$) and the heat generation (I^2R). According to Fourier effect, a temperature gradient exists between the hot side and the cold side; there will be a heat conduction rate defined as :

$$Q_T = K(T_h - T_c) ,$$

from the hot side to the cool side. Therefore, including Peltier effect, Joule effect and heat conduction, the heat generation rate of the hot side is:

$$Q_h = \alpha T_h I + I^2 R / 2 - K(T_h - T_c) . \quad (2-2)$$

The same way, the heat pump rate of the cold side is:

$$Q_c = \alpha T_c I - I^2 R / 2 - K(T_h - T_c) . \quad (2-3)$$

According to energy conservation, it has $Q_h = Q_c + P_{input}$ and because of Seebeck effect, it has

$$U = IR + \alpha \Delta T . \quad (2-4)$$

2.3.2. Structure of the Calorimeter

The calorimeter is designed using two TEMs, and the battery is placed between the two TEMs like a sandwich. The heat sink is directly open to the environment and a fan is used to accelerate the air flow. The designed calorimeter is a symmetrical system, which half structure of the designed calorimeter is shown in Figure 12

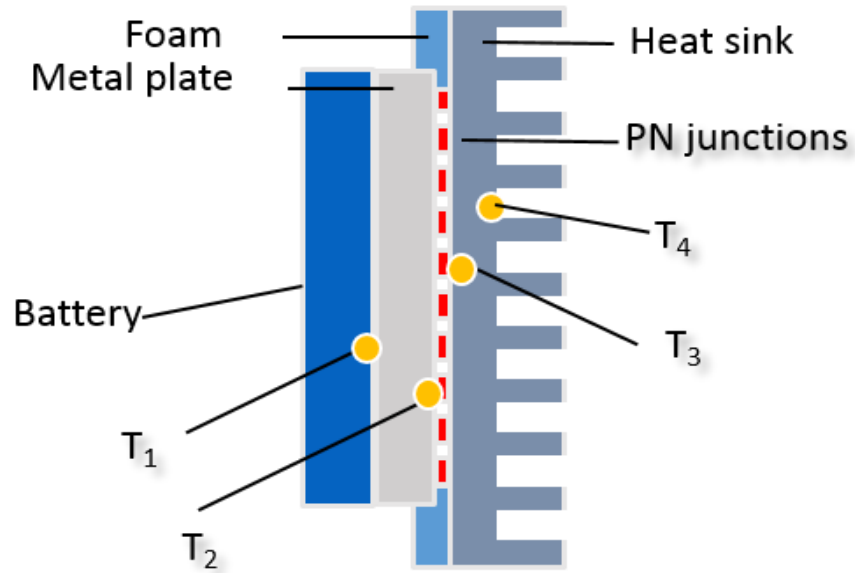


Figure 11: Structure of part the calorimeter

,where T_1 is the temperature of the metal plate in the battery side, T_2 is the temperature of the metal plate in the P-N junction side, T_3 is the temperature of the hot side of the P-N junction. T_4 is the temperature of the heat sink.

The cold side of the TEM is in contact with a metal plate and the metal plate is in contact with the battery. Between the battery and the metal plate, a carbon-based thermal sheet (Not shown in the figure) is used to minimize the thermal resistance. A heat sink is in contact to the hot side of the TEM, and a fan (Not shown in the figure) is used to speed up the air flow to increase the heat exchange. The foam is used to thermally insulate the designed calorimeter from the ambient.

The heat generated by the battery goes through the metal plate and is pumped out by the TEM. The battery test station controls the current that is applied to the TEM to control the heat pump rate, so that the designed calorimeter can maintain the battery under a normal operating temperature even though there is large heat generation rate produced by the battery during charging and discharging.

2.4. Modeling of the Calorimeter

TEMs have been widely used in many applications to control the temperature of an object. Some researchers used TEM to cool the object below the ambient temperature or maintain the object at a constant temperature [22] [23] [24]. In order to estimate the heat generation rate of the battery and control the temperature of the TEM and the battery. A mathematical model of the TEM should be built. However, it is difficult to determine the model of the TEM because of nonlinear behavior of the TEM. In order to solve the problem, finite element model and finite difference model have been proposed [25] [26]. Neto presented a second order discrete time autoregressive moving average model to describe the behavior of the TEM [27]. However, these models are still complex to be used to design the controller and implement into the test station.

In this paper, a simple and concise model considering the nonlinear characteristics of the TEM has been proposed. A first order heat conduction model is constructed and transforms into Laplace domain to design the controller using Simulink. Then the model is transformed into a state space form and discretized to develop a heat estimation algorithm.

2.4.1. Parameters identification of TEM

It has been mentioned earlier that the heat pump rate of the TEM is a function of the current and the temperature of the cold and hot side of the P-N junction (Equation (2-2)). Therefore, we defined the heat pump rate as:

$$Q_{pump} = k_1 T_2 I_{TEM} - k_2 I_{TEM}^2 - k_3 (T_3 - T_2), \quad (2-5)$$

where I_{TEM} is the current that applied to the TEM and k_1 , k_2 and k_3 are constants that should be determined. However, we cannot place thermocouples between the cold side of the P-N junction and the metal plate to measure T_2 or between the hot side of the P-N junction and the heat sink to

measure T_3 . We can only measure the temperature of the metal plate in the battery side T_1 and the temperature of the heat sink T_4 that is in contact with the hot side of the P-N junction. Even though there is a temperature difference between the heatsink and the hot side of P-N junction, because the thermal conductivity of the heatsink is very large, we can approximately assume that T_3 is the same as T_4 . In order to make T_4 closer to T_3 , we used a copper shelter that has the same surface area to cover the thermocouple which placed at the center of the heat sink. In this way, the shelter can prevent the air flowing and decrease the heat dissipation only at the thermocouple area, so that it cannot influence the whole heat dissipation of the heat sink. For T_2 , it can be calculated based on a thermal conduction model of the metal plate.

We divide the metal plate into two control volumes. A PCB is used instead of the battery to calculate the heat generation rate (Q_{PCB}): $Q_{PCB} = I_{PCB}^2 R_{PCB}$, where I_{PCB} is the current applied to the PCB and R_{PCB} is 0.5Ω , as shown in Figure 12.

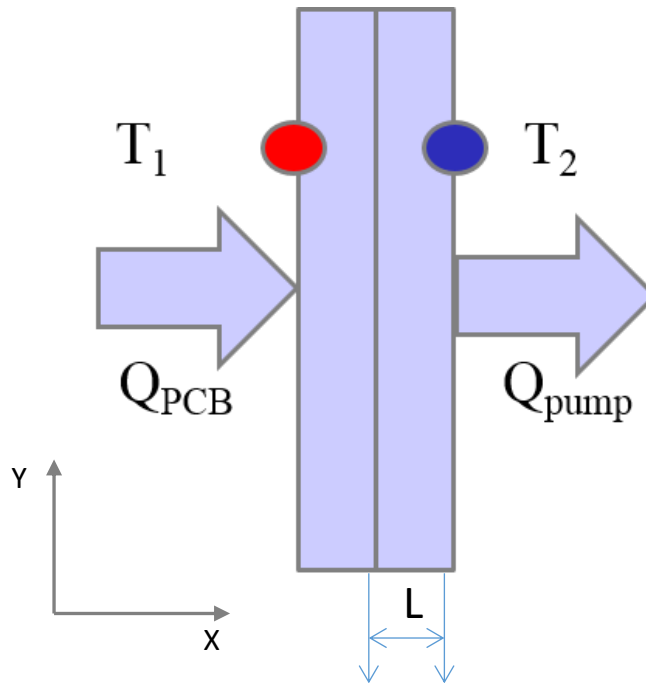


Figure 12: Control volumes of the metal plate

The coefficient of k_1, k_2, k_3 are need to be determined. In general, the thermal model of the metal plate is formulated based on the thermal energy balance in a control volume:

$$\rho C_p \frac{\partial T}{\partial t} = k_x \frac{\partial^2 T}{\partial x^2} + k_y \frac{\partial^2 T}{\partial y^2} + k_z \frac{\partial^2 T}{\partial z^2} + q''' , \quad (2-6)$$

where q''' is described by a volumetric heat source (W/m^3). In this thesis, we assumed that the heat generated by the PCB all goes into the metal plate that is insulated with a soft foam. In addition, there is no internal heat source inside the metal plate, so the heat conduction in y and z-direction and q''' is equal to 0. Then equation (2-6) becomes:

$$\alpha \frac{\partial^2 T}{\partial x^2} = \frac{\partial T}{\partial t} , \quad (2-7)$$

where $\alpha = k_x / (\rho C_p)$ is the thermal diffusivity of the material, and then we assumed that $T(x,t) = U(x)V(t)$. It has:

$$\frac{\alpha \partial^2 U}{U \partial x^2} = \frac{1}{V} \frac{\partial V}{\partial t} \Rightarrow \frac{\alpha \partial^2 U}{U \partial x^2} = \frac{1}{V} \frac{\partial V}{\partial t} \Rightarrow \frac{U''}{U} = \frac{V'}{\alpha V} . \quad (2-8)$$

Solving the equation (2-8), we have:

$$U = A \cos(\beta x) + B \sin(\beta x) , V = C e^{-\beta^2 \cdot \alpha \cdot t} , \quad (2-9)$$

$$T = (A \cos(\beta x) + B \sin(\beta x)) e^{-\beta^2 \cdot \alpha \cdot t} , \quad (2-10)$$

where, A and B are integration constants, β can be regarded as exponentially decaying constant. Equation (2-10) describes the temperature profile of the metal plate with time and position. In reality, we can only measure the temperature at $x=0$, and we do not need to analyze the temperature of all the points within the metal plate. So we focused on the temperature at point $x=0$. Equation

(2-10) becomes: $T = Ce^{-\beta^2\alpha}$. In order to use the model for designing of the controller and Kalman Filter, a state space form of the model is derived.

In order to estimate the temperature profiles at the surface of the metal plate, the values of the thermal diffusivity, length, surface area of the metal plate are needed. The metal plate is made of aluminum, which the parameters are shown in the following table.

Table 4. Characteristics of Aluminum.

Thermal conductivity(W/(m· K))	100
Density(kg/m ³)	2700
Specific heat capacity(J/(kg· K))	897

α is calculated based on the Table 4, and the result is $\alpha = 4.13 * 10^{-5} \text{ m}^2/\text{s}$. The length of the metal plate L is indicated from the specifications of the thermoelectric assembly, $1.85 * 10^{-2} \text{ m}$. The characteristic time, t is read from the following figure.

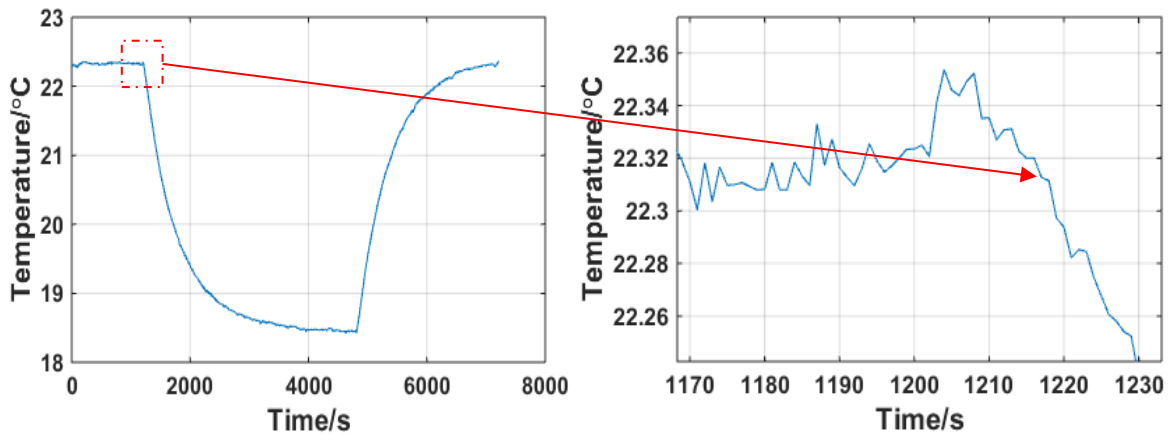


Figure 13: Determine the characteristic time

Figure 13 shows that when a 20W heat pump rate is applied on the one side of the metal plate at the 1202 second, the surface temperature of the other side begins to decrease at the 1208 second. Therefore, the characteristic time of the metal plate is 6 seconds. Then the thermal Fourier

number of the metal plate is calculated by using $F_{oh}=(\alpha t)/L^2$. And the result is 0.72, which is much larger than 0.2.

Therefore, according to Figure 12, the metal plate is considered as two control volumes, we derive the equation based on the left control volume:

$$\rho C_{\rho} V_1 \frac{dT_1}{dt} = Q_{PCB} + k \cdot A \cdot \frac{T_2 - T_1}{L},$$

where C_{ρ} is the heat capacity of the metal plate, V_1 is control volume of the left side of the metal, k is the conductive coefficient, A is the area of the metal plate, and L is the distance between the two control volumes. Likewise, we derive the following equation based on the right side of the metal plate:

$$\rho C_{\rho} V_2 \frac{dT_2}{dt} = Q_{pump} + k \cdot A \cdot \frac{T_1 - T_2}{L},$$

where V_2 is control volume of the right side of the metal plate.

In order to simplify the equations, V_1 is the same as V_2 in ideal and k , A and L are all constant.

Therefore, we define that $K = \frac{(k \cdot A)}{L}$ with the unit (W/K) and $\rho C_{\rho} V_1 = \rho C_{\rho} V_2 = C_M m_M$ with the

unit (J/K). Then the two equations can be rewritten as follows:

$$(C_M m_M) \dot{T}_1 = Q_{PCB} - K (T_1 - T_2). \tag{2-11a}$$

$$(C_M m_M) \dot{T}_2 = K (T_1 - T_2) - Q_{pump}. \tag{2-11b}$$

Rearranging the equation (2-11), we can get equation (2-12) and equation (2-13):

(2-12)

$$T_2 = \frac{(C_M m_M) \dot{T}_1 + K T_1 - Q_{PCB}}{K},$$

(2-13)

$$T_1 = \frac{(C_M m_M) \dot{T}_2 + K T_2 + Q_{pump}}{K},$$

where C_M is the heat capacity of the metal plate for the control volume, m_M is the mass of the metal plate for a control volume, K is presented as $\frac{kA}{L}$, Q_{pump} is the heat pump rate of the TEM, and Q_{PCB} is the heat generation rate of the PCB.

From the equation (2-12) and (2-13), the initial condition is $T_1 = T_2 = T_{initial}$ (shown in Figure 14), and when in steady state:

(2-14a)

$$T_{2working} = T_{initial} - \frac{Q_{PCB}}{K},$$

(2-14b)

$$T_{1working} = T_{initial} + \frac{Q_{pump}}{K},$$

where $T_{1working}$ and $T_{2working}$ are steady state of the metal plate temperature in PCB and TEM side, respectively. It means that when the PCB is generating heat and the TEM is working to pump out heat, there occurs a temperature gradient in the metal plate. The temperature of the metal plate in PCB side (T_1) is measurable, but the temperature of the metal plate in P-N junction side (T_2) is not measurable. Under the condition that $Q_{PCB} = Q_{pump}$, we can calculate $T_{2working}$:

(2-15)

$$T_{2working} = 2T_{initial} - T_{1working}.$$

In order to make $Q_{PCB} = Q_{pump}$, we applied a certain current to the PCB to make Q_{PCB} as a constant, then applied different constant current to the TEM (changing Q_{pump}) at the same time,

and made sure that the final value of T_1 is equal to the initial value of T_1 . The results are shown in Figure 14.

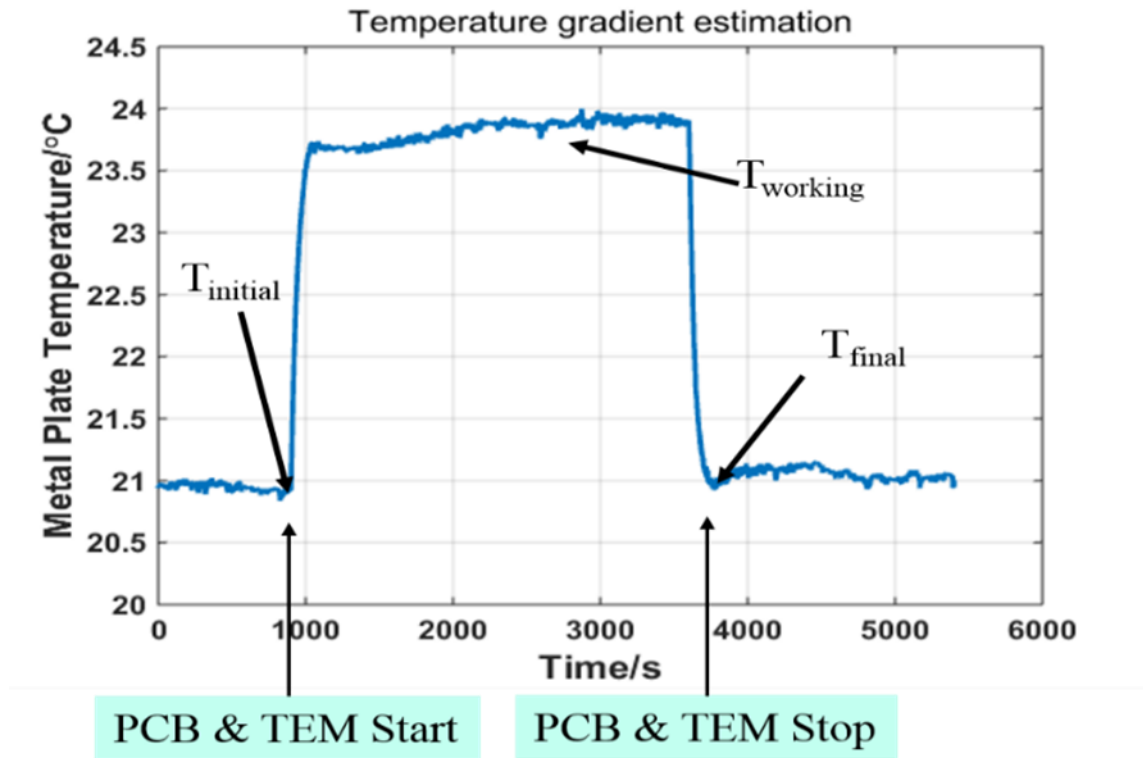


Figure 14: Temperature profile of metal plate in PCB side

The temperature profile of the metal plate in the PCB side shows that the initial temperature of T_1 is 21°C that is the same as the ambient temperature. When the PCB and the TEM begin working at the same time, the temperature of the metal plate in the PCB side rises up and stabilizes at 23.78°C . When the current is cut off to the PCB and the TEM at the same time, T_1 fall to 21°C exactly. We assume that the whole thermal system is well insulated so that the average temperature of the metal plate does not change during this process and the total heat generation of the PCB is all pumped out by the TEM. Within the same period, $Q_{\text{pump}}=Q_{\text{PCB}}$. The recorded data is shown in Table 5.

Table 5: Parameters identification of TEM

I_{PCB} (A)	Q_{pump} (W)	I_{TEM} (A)	$T_{2working}$ ($^{\circ}C$)	$T_{3working}$ ($^{\circ}C$)
4	8.0	0.17	20.14	21.60
5	12.5	0.29	21.36	22.81
6	18.0	0.43	19.40	21.62
7	24.5	0.64	19.60	22.43
8	32.0	0.84	18.94	22.76
9	40.5	1.09	17.98	23.06
10	50.0	1.45	17.55	23.79
11	60.5	1.84	16.65	24.74
12	72.0	2.30	15.29	25.44
13	84.5	3.08	15.72	28.03
14	98.0	4.09	15.70	31.51

$T_{2working}$ in Table 5 is calculated by equation (2-15), and Q_{PCB} is calculated by $Q_{PCB} = I_{PCB}^2 R_{PCB}$ where R_{PCB} is equal to 0.5Ω . The other three variables are measured directly.

Least squares method is employed to fit the data into equation (2-5):

$$Q_{pump} = k_1 T_2 I_{TEM} - k_2 I_{TEM}^2 - k_3 (T_3 - T_2)$$

Then, we can obtain $k_1=0.166$ (V/K) , $k_2=4.587(\Omega)$, $k_3=1.5(W/K)$. Then equation (2-5) becomes:

$$Q_{pump} = 0.166 \cdot T_2 \cdot I_{TEM} - 4.587 \cdot I_{TEM}^2 - 1.5 \cdot (T_2 - T_3). \quad (2-16)$$

According to equation (2-16), there are three terms in Q_{pump} . The first term represents the heat pump rate by Peltier effect. The second term represents the Joule heating generation. The third term represents the Fourier heat conduction.

Now, we have obtained an experimental equation of the heat pump rate of the TEM based on the current applied to it and the temperature measured by the thermocouples. We can put the data in Table 5 into the experimental equation (2-16) and compare with Q_{PCB} in Figure 15. indicates that the identified coefficients are close to the measured value with the error that is less than 5%.

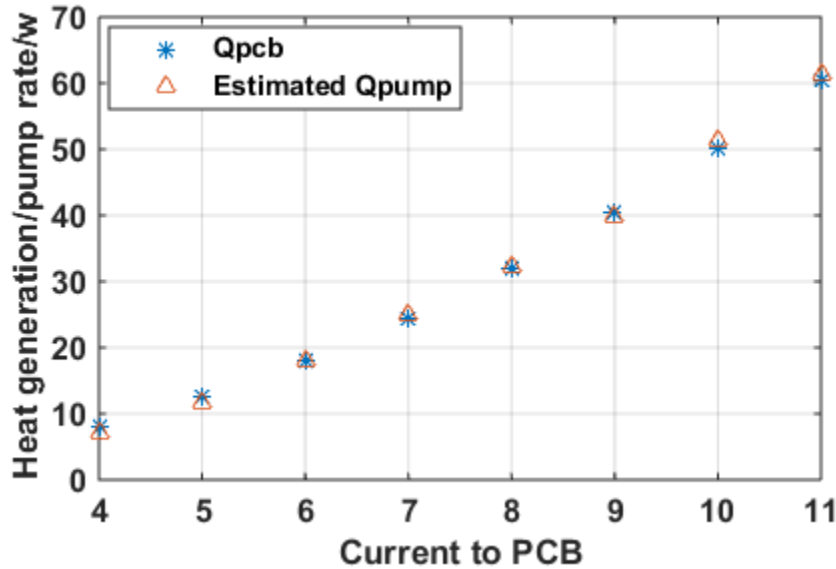


Figure 15: Comparison of experimental values and estimated value

After determining the heat pump rate of the TEM, the heat capacity and the thermal conductivity of the metal plate remain to be identified.

2.4.2. Identification of thermal parameters of the metal plate

When plugging equation (2-13) into equation (2-12), we obtain the equation:

$$-Q_{\text{pump}} - ((C_M m_M) \dot{T}_1 + K T_1 - Q_{\text{PCB}}) + K T_1 = \frac{(C_M m_M)^2 \ddot{T}_1 + K (C_M m_M) \dot{T}_1 - C_M m_M \dot{Q}_{\text{PCB}}}{K}$$

Rearranging the equation, it becomes:

$$\frac{(C_M m_M)^2}{K} \ddot{T}_1 + 2C_M m_M \dot{T}_1 + Q_{pump} - Q_{PCB} - \frac{C_M m_M \dot{Q}_{PCB}}{K} = 0. \quad (2-17)$$

In order to solve equation (2-17), we assume that $Q_{PCB} = Q_{pump}$ and in the steady state, \dot{Q}_{PCB} is equal to 0. Equation (2-17) becomes:

$$\frac{(C_M m_M)^2}{K} \ddot{T}_1 + 2C_M m_M \dot{T}_1 = 0. \quad (2-18)$$

This is a second order ordinary differential equation (ODE), and the solution for this equation has the following form:

$$T_1(t) = T_1(0) + \frac{C_M m_M}{2K} (1 - e^{\frac{-2K}{C_M m_M} t}) \cdot \dot{T}_1(0), \quad (2-19)$$

where $T_1(0)$ and $\dot{T}_1(0)$ are initial values for three different intervals. The unknown initial value $T_1(0)$ is obtained from the experimental data. $\dot{T}_1(0)$ is calculated backwards based on comparison between the experimental data and the equation (2-19). With the least squares method: $2K / C_M m_M = 0.022s^{-1}$.

Table 6 The initial values of the solution for equation (2-18)

	T_1 (° C)	$\dot{T}_1(0)$ (° C/s)
Initial State	22.21	0
Working State	22.16	-0.027
After Working	23.03	0.024

The following figure shows the comparison between the experimental data and calculation.

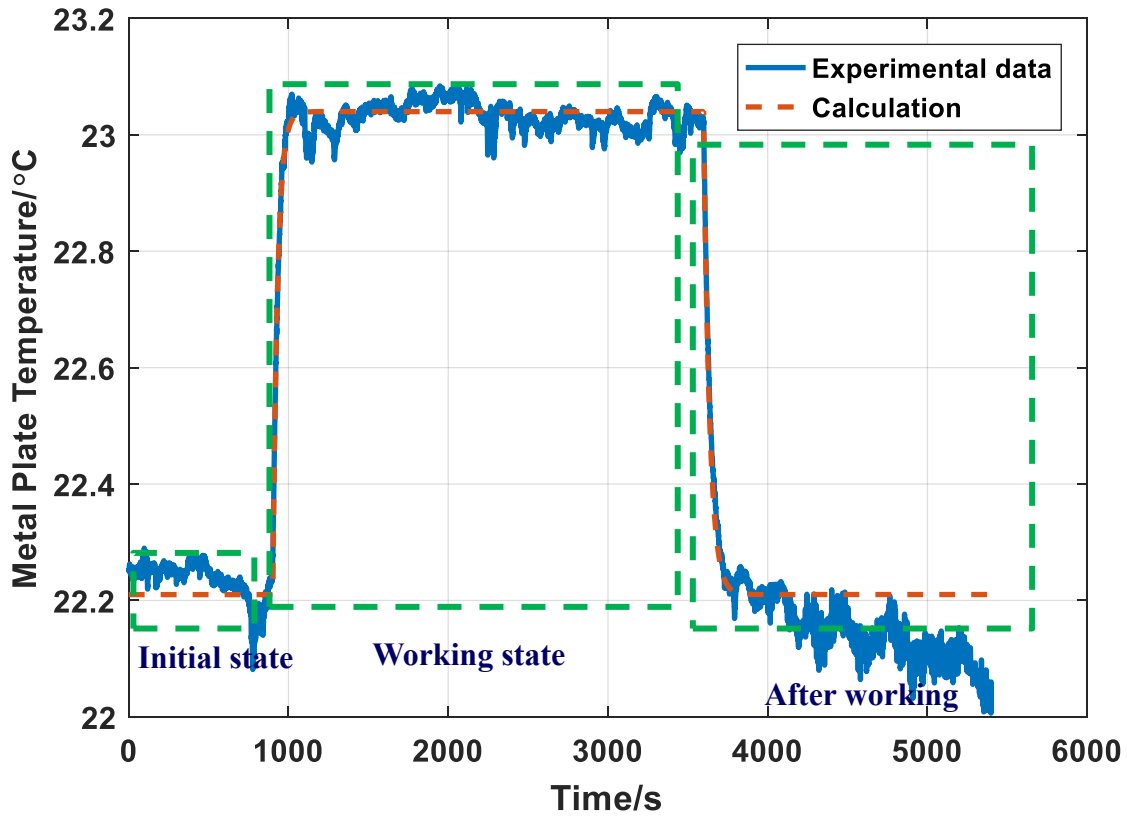


Figure 16: Comparison between experimental data and equation (2-19)

K can be determined when the metal plate is in the steady state. The control volume in the PCB side is shown in Figure 12, based on the energy balance theory, the heat flux flows into the control volume should be equaled to the heat flux that flows out in the unit area. Therefore, when in the steady state equation (2-20) results as follows:

$$Q_{PCB} = K(T_{1working} - T_{2working}). \quad (2-20)$$

When plugging equation (2-15) into equation (2-20), K can be determined by the following equation:

(2-21)

$$K = \frac{Q_{PCB}}{2(T_{1working} - T_{initial})}$$

Q_{PCB} can be calculated by Ohm's law and $T_{1working}$, $T_{initial}$ are listed in Table 7: Data used for determining K .

Table 7: Data used for determining K

Q_{PCB} (W)	$T_{1working}$ ($^{\circ}C$)	$T_{initial}$ ($^{\circ}C$)	K (W/K)
8.0	22.02	21.50	7.69
12.5	23.02	22.19	7.53
18.0	22.22	20.81	6.38
24.5	22.60	21.10	8.16
32.0	23.02	21.07	8.20
40.5	23.88	20.93	6.86
50.0	24.35	20.95	7.35
60.5	25.89	20.97	7.00
72.0	26.45	20.87	6.45
84.5	27.26	21.49	7.32
98.0	28.26	21.89	7.80

Calculating the average value of K and we can finally determine the thermal conductivity of the metal plate to be 7.34 W/K. K and $K/C_M m_M$ have already been calculated, and the product of the heat capacity and the mass of the metal plate C_{MM} then can be calculated. According to the 11 sets of the experimental data and then calculating the average value of C_{MM} , C_{MM} is equal to 670J/K.

2.4.3. Model Validation

After determining the heat capacity and the thermal conductivity of the metal plate, the forward difference method is used to discretize the model of the metal plate. Then equation (2-11) becomes:

$$Q_{PCB}^k - K(T_1^k - T_2^k) = C_M m_M \frac{T_1^{k+1} - T_1^k}{\Delta t}, \quad (2-22a)$$

$$K(T_1^k - T_2^k) - Q_{pump}^k = C_M m_M \frac{T_2^{k+1} - T_2^k}{\Delta t}, \quad (2-22b)$$

where Δt is the sampling time that is 0.5s.

Then rearranging equation (2-22) to obtain equation (2-23):

$$T_1^{k+1} = \frac{\Delta t}{C_M m_M} Q_{PCB}^k + \left(1 - \frac{\Delta t K}{C_M m_M}\right) T_1^k + \frac{\Delta t K}{C_M m_M} T_2^k, \quad (2-23a)$$

$$T_2^{k+1} = -\frac{\Delta t}{C_M m_M} Q_{pump}^k + \left(1 - \frac{\Delta t K}{C_M m_M}\right) T_2^k + \frac{\Delta t K}{C_M m_M} T_1^k. \quad (2-23b)$$

Recall equation (2-23) in state space form:

$$\begin{bmatrix} T_1^{k+1} \\ T_2^{k+1} \end{bmatrix} = \begin{bmatrix} 1 - \frac{K\Delta t}{C_M m_M} & \frac{K\Delta t}{C_M m_M} \\ \frac{K\Delta t}{C_M m_M} & 1 - \frac{K\Delta t}{C_M m_M} \end{bmatrix} \begin{bmatrix} T_1^k \\ T_2^k \end{bmatrix} + \begin{bmatrix} \frac{\Delta t}{C_M m_M} & 0 \\ 0 & -\frac{\Delta t}{C_M m_M} \end{bmatrix} \begin{bmatrix} Q_{PCB}^k \\ Q_{pump}^k \end{bmatrix} \quad (2-24)$$

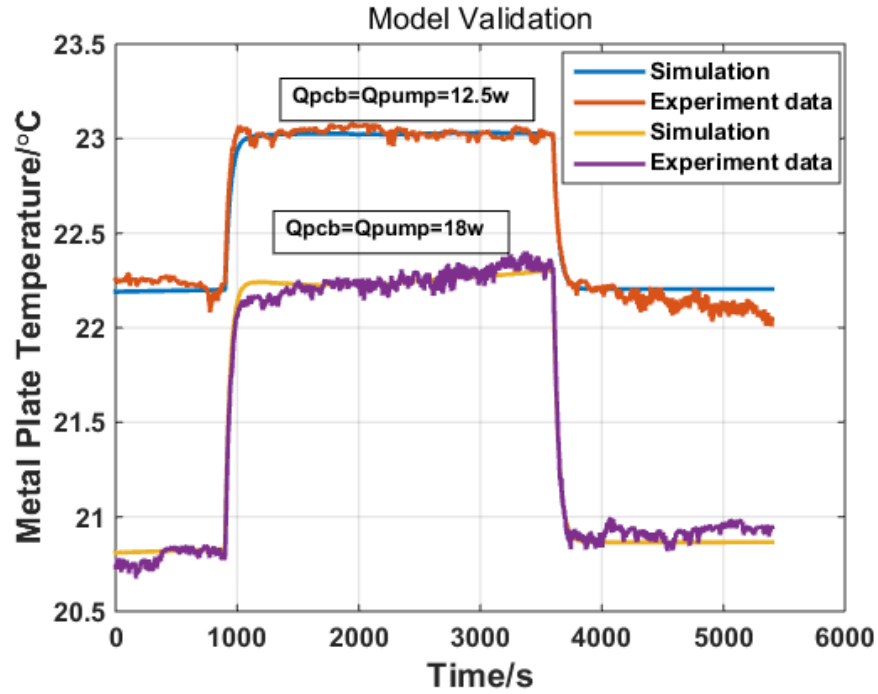


Figure 17: Model validation

All the parameters in the equation (2-23) are known and using MATLAB to simulate equation (2-23). Figure 17 shows two sets of experimental data with different heat generation rate of the PCB and different initial values of the temperature of the metal plate in the PCB side. The two sets of the experimental data from the battery test station are compared with the simulation results calculate by MATLAB based on equation (2-23).

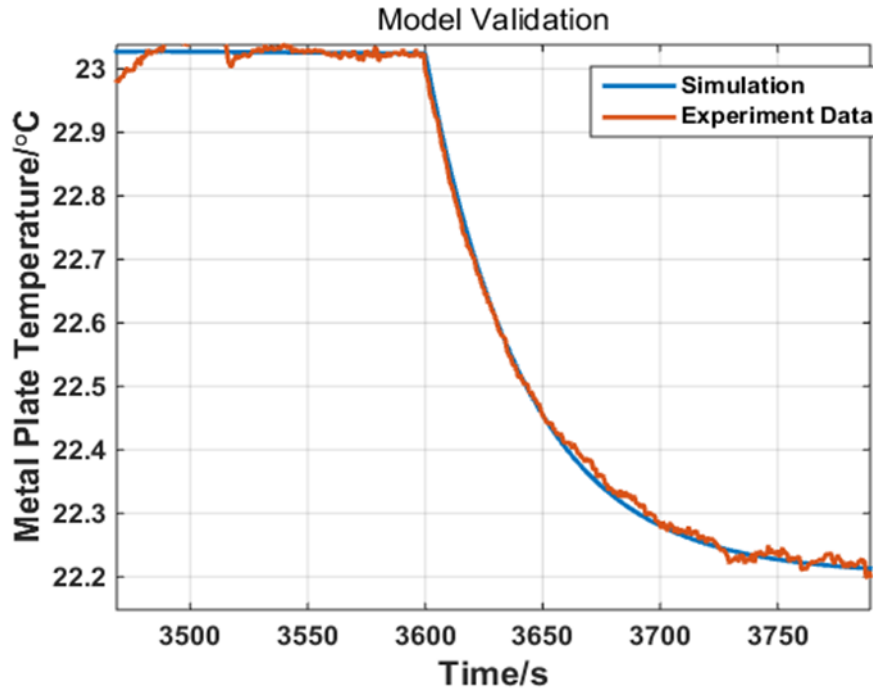


Figure 18: Expanded view of the transient behaviors

From the Figure 17: Model validation and Figure 18, the simulation results with the identified parameters are very close to the temperature profile of the metal plate that is measured by the battery test station. During 0 to 900s, where no current is applied to the PCB and the TEM, the metal plate temperature is the same as the ambient temperature that varies within 0.2°C. The PCB begins to generate heat at 900s, and the TEMs begin to pump out heat at the same time. The heat generation rate of the PCB is equal to the heat pump rate of the TEMs. After around 200s, the temperature of the metal plate enters the steady state. The current that is applied to the PCB and the TEMs are stopped at 3600s. The temperature of the metal plate falls back to the ambient temperature, meaning that the average temperature of the whole metal plate is the same as the ambient temperature during the working period and the rest period. When in the steady state, the experimental data and simulation reaching the same temperature means that the thermal conductivity of the metal plate determined is correct. When the current stops to flow to the PCB and TEM, the temperature drops in the same pattern, meaning that the time constant (τ) of the

metal plate is determined correctly. Recalling equation (2-22), when the thermal conductivity and the time constant are determined, then the heat capacity can be determined. The simulation results match the experimental data well.

3. Dynamic calibration of the calorimeter

3.1. Design of a temperature controller

3.1.1. Review of linear controllers

Proportional controller (P), integral controller (I), derivative controller (D), and lead-lag compensator are widely used in industry, especially a well-known structure for the control form: proportional plus integral plus derivative control (PID). The advantages of the PID controller are to control a system without any mathematical model and tune the parameters manually. The algorithm is:

$$u(t) = K_P e(t) + K_I \int_0^t e(t) dt + K_D \frac{de(t)}{dt}, \quad (3-1)$$

where $u(t)$ is the output of the controller. K_P , K_I , and K_D are the proportional gain, integral gain, and derivative gain, respectively. All the three gains are the turning parameters. Several tuning methods like Ziegler-Nichols method, Tyrus-Luyben method can be used to tune the gains online. Table 6 summarizes the effect of the parameters independently. $e(t)$ is the error that equals to the reference value ($RV(t)$) minus the processing variable ($PV(t)$):

$$e(t) = RV(t) - PV(t).$$

The corresponding transfer function of equation (3-1) is:

$$D(s) = K_P s + \frac{K_I}{s} + K_D s \quad (3-2)$$

Steady-error (e_{ss}), rise time (t_r), settling time (t_s), and overshoot (M_p) are the four important specifications for a control system design.

Table 8: Effect of the parameters

	K_P	K_I	K_D
e_{ss}	Decrease	Eliminate	No effect
t_r	Decrease	Decrease	Depended on Plant
t_s	Depend on Plant	Increase	Decrease
M_p	Increase	Increase	Decrease

Even though PID controller is powerful and widely used, under some conditions, a satisfactory design of process dynamics cannot be obtained by adjusting the gains alone. Therefore, a compensation of the process dynamics is necessary. A compensator is based on the system plant that can improve the frequency response of the system. The compensator works by putting poles and zeros on the root locus of the system to optimize the system response including steady state error, rising time, overshoot, and settling time. The transfer function of a compensator in the Laplace domain can be written as:

$$D(s) = \frac{Js + 1}{aJs + 1}, \quad (3-3)$$

where J is a constant, and if $a > 1$, the compensator is called a lead compensator which functions as a PD controller, so it is also called PD compensator; if $a < 1$, the compensator is called a lag compensator as a PI compensator.

Lead compensator is used to determine the system response and increase its stability. Lag compensator can improve the steady-state response of the system but decrease the speed of response. Therefore, in order to meet the requirements of the desired system, a lead compensator,

and a lag compensator sometimes are group together and construct a lead-lag compensator that not only enhances the stability but also improves the response. A lead-lag compensator means that two poles and two zeros are needed. The transfer function of a lead-lag compensator is as:

$$D(s) = K_D \frac{(s - z_1)(s - z_2)}{(s - p_1)(s - p_2)}, \quad (3-4)$$

where K_D is a proportional gain, z_1 and z_2 are two zeros, p_1 and p_2 are two poles which satisfied $|p_1| > |z_1| > |z_2| > |p_2|$.

3.1.2. Selecting the controller

The most notable advantage of the PID controller is that the parameters can be turned without the system plant. However, tuning a PID controller's parameters needs a plenty of experience and is time-consuming. In addition, the performance of the D controller usually is very poor because of its noise sensitivity. The thermal model of the metal plate is used to design the compensator. The most important thing is a fast response of the system that is considered for design of the controller.

From equation (2-10), we can rewrite it in a transfer function form:

$$G_2 = \frac{T_1(s)}{Q_{PCB}(s)} = \frac{K}{C_M m_M^2 s^2 + 2C_M m_M Ks}, \quad (3-5)$$

$$G_1 = \frac{T_1(s)}{Q_{pump}(s)} = -\frac{K}{C_M m_M^2 s^2 + 2C_M m_M Ks}, \quad (3-6)$$

$$\frac{T_2(s)}{Q_{pump}(s)} = -\frac{K + C_M m_M s}{C_M m_M^2 s^2 + 2C_M m_M Ks}, \quad (3-7)$$

(3-8)

$$\frac{T_2(s)}{Q_{PCB}(s)} = \frac{K + C_M m_M s}{C_M m_M^2 s^2 + 2C_M m_M K s}$$

Therefore, we obtain the system plant and can use a parameter tuner software that inserts in MATLAB to determine the parameters of the controllers.

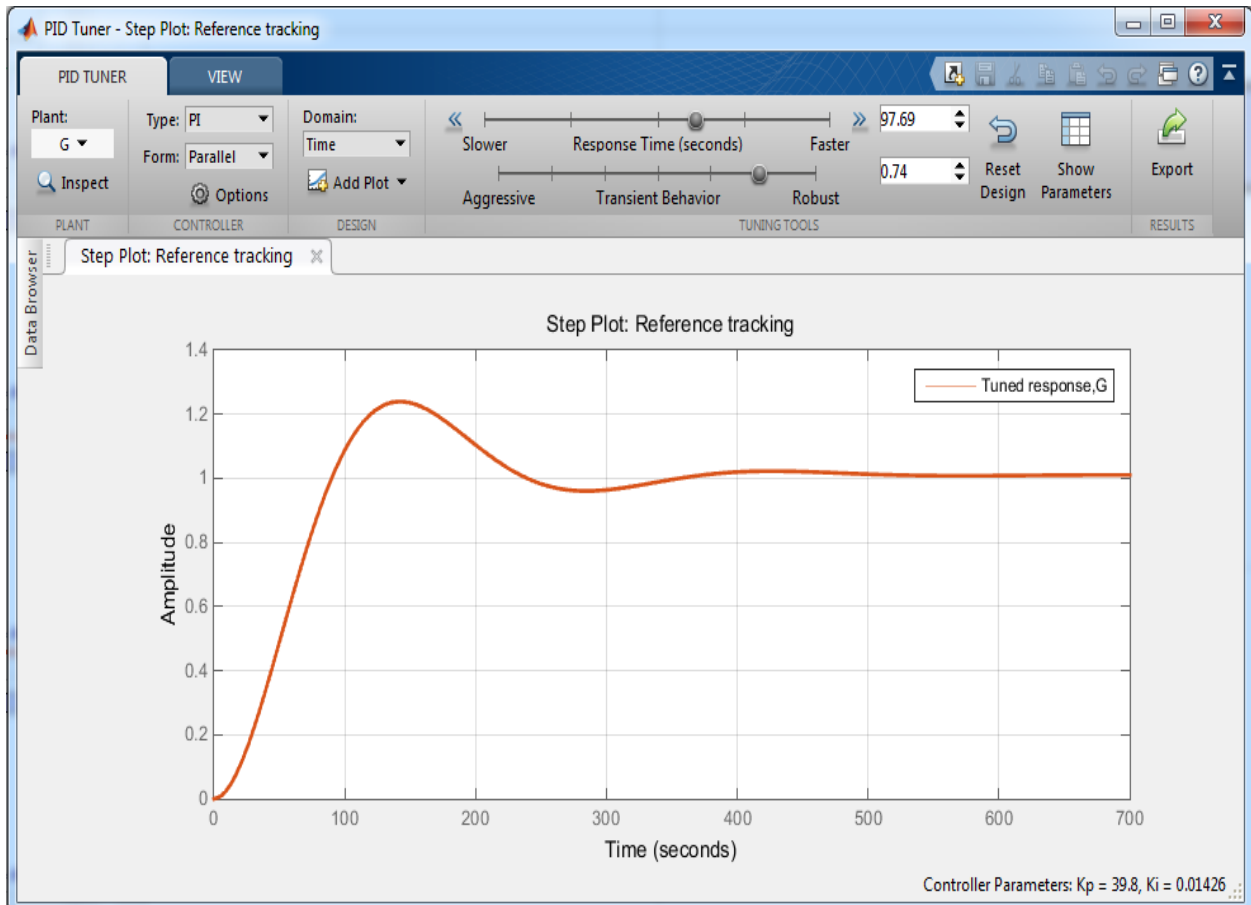


Figure 19: A screenshot of parameter tuner

Figure 19 shows that when a plant is imported into the software, you first can select what kind of the controller or compensator that you want to choose, then tuning the parameters to see the response of the system. The requirements of the desired controller or compensator that need to be applied in the battery test station including the overshoot of the system response needs to be less than 20%; the rising time is less than 120s, and no steady error. A PI, PID controller, lead

compensator, lag compensator, and lead-lag compensator are tested. A block diagram of selecting a controller is shown in Figure 19.

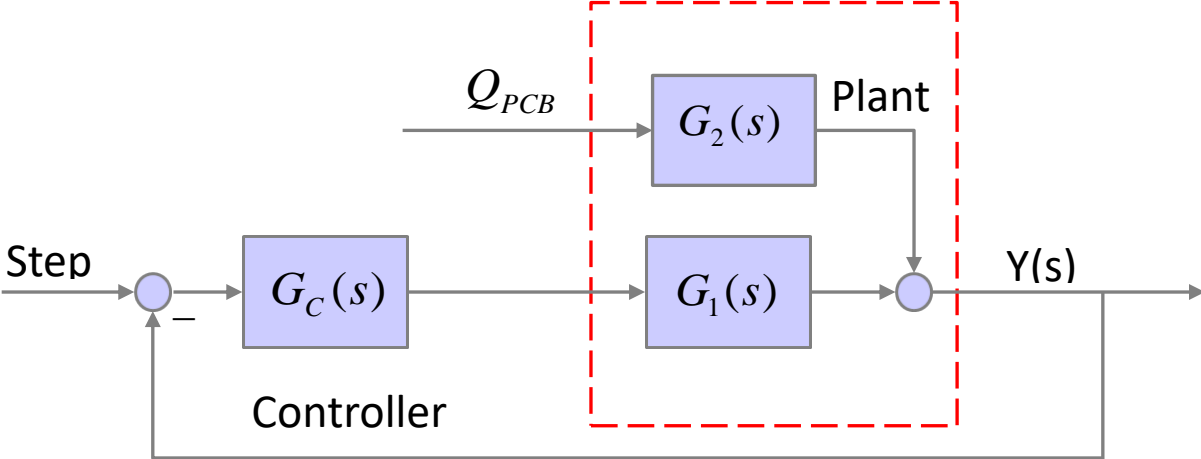


Figure 20: Block diagram for controller and TEM

In this block diagram, we regard the heat generation of the PCB as a disturbance of the system, and is set to 0. $Y(s)$ is the response of the system, $G_1(s)$ and $G_2(s)$ are the system plants. After tuning an optimized parameter of each controller, the response of the system with different controllers and compensator are shown in Figure 21.

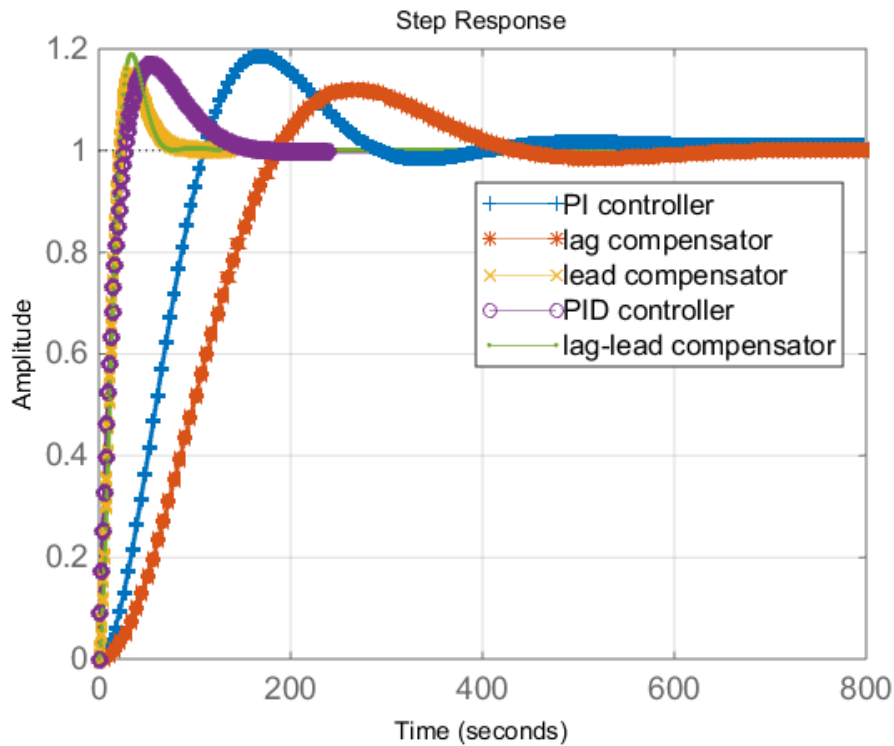


Figure 21: Step response of the system with different controllers

The figure shows clearly that the lead-lag compensator and the lead compensator have a faster response compare to other controllers with the overshoot less than 20%.

There are two commonly used quantities that measure stability margin related to the stability criteria: phase margin (PM) and gain margin (GM). The GM and the PM can be read directly from the Bode plot. GM is the value of the vertical distance between the magnitude curve and the magnitude curve equal to 0 dB at the frequency where phase curve is equal to 180° . PM is an alternative way to test the stability of a system, it is defined as the value that the phase exceeds -180° when magnitude curve is equal to 0 dB. When $GM < 0$, it indicates that the system is unstable while $PM > 0$ indicates the system is stable. Figure 22 and Figure 23 shows the Bode plot of the lead compensator and the lead-lag compensator. From the two figures, we can find that the value

of GM of the lead-lag compensator is larger than the lead compensator. Therefore, the lead-lag compensator is more stable than that of the lead compensator.

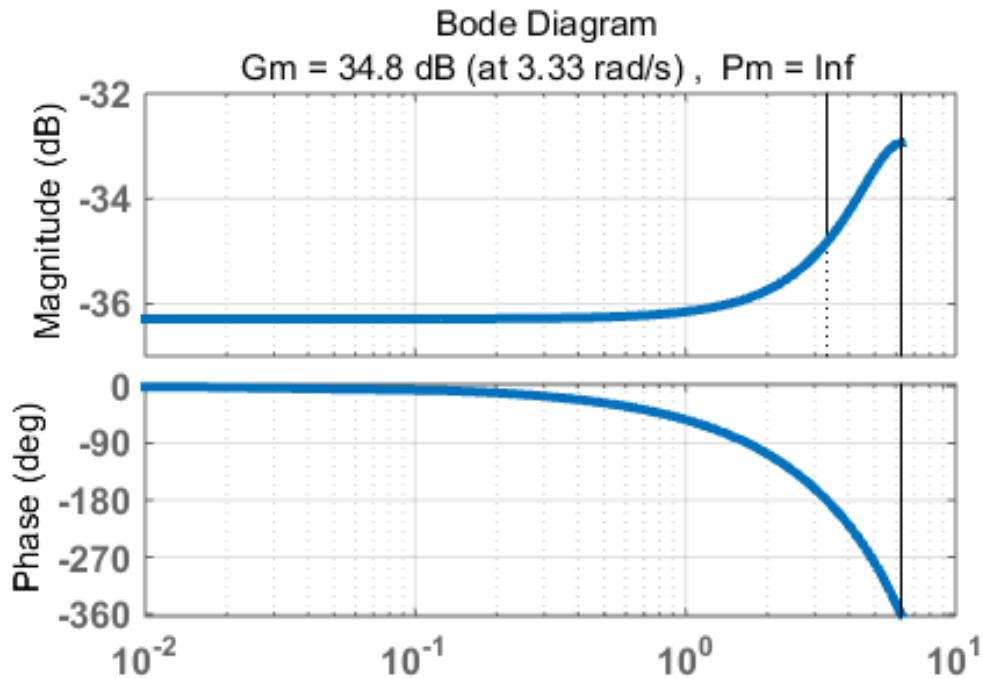


Figure 22 The Bode plot of the lead compensator

After the comparison with the step response and the stability, a lead-lag compensator is selected to be the controller for controlling the temperature of the calorimeter.

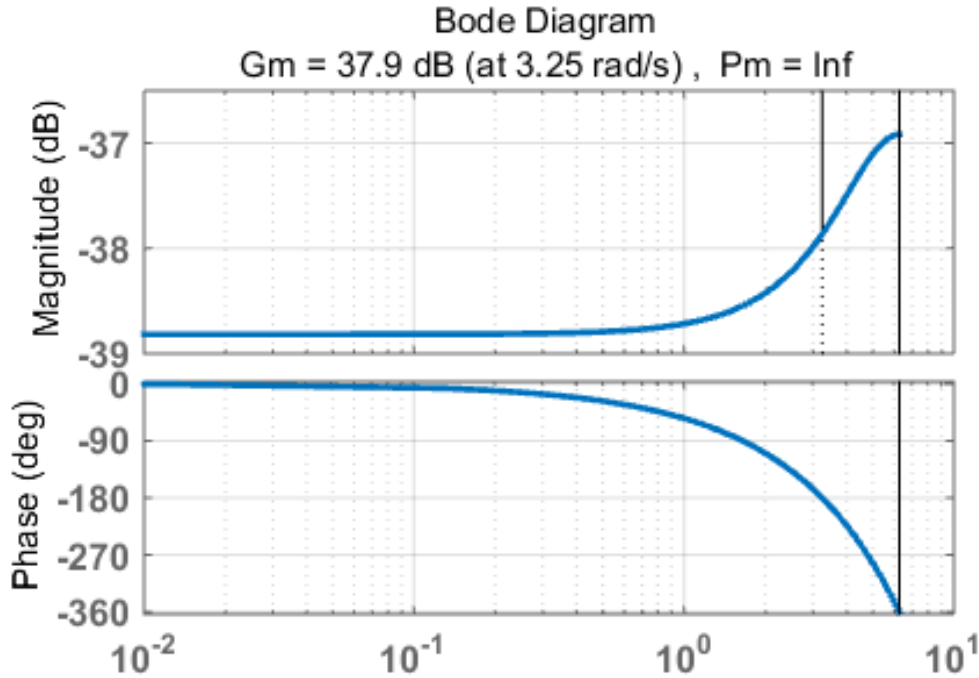


Figure 23: The Bode plot of the lead-lag compensator

3.1.3. Implement of the lead-lag compensator

The lead-lag compensator in the Laplace domain cannot be directly implemented into LabVIEW. Therefore, we have to discretize it. The compensator $G_C(s)$ is expressed as:

$$G_C(s) = \frac{Q(s)}{E(s)} = K_p \frac{(1 + a_1s)(1 + a_2s)}{(1 + b_1s)(1 + b_2s)},$$

where $Q(s)$ is an output of the compensator that is the heat pump rate applied to the metal plate. $E(s)$, the voltage signal, is the input of the compensator. First, the Laplace function is transformed into the time domain:

$$\frac{Q(s)}{E(s)} = K_p \frac{a_1a_2S^2 + (a_1 + a_2)S + 1}{b_1b_2S^2 + (b_1 + b_2)S + 1}$$

↓

$$b_1 b_2 S^2 Q(s) + (b_1 + b_2) S Q(s) + Q(s) = K_p a_1 a_2 S^2 E(s) + K_p (a_1 + a_2) S E(s) + K_p E(s)$$

↓

$$b_1 b_2 \ddot{Q}(t) + (b_1 + b_2) \dot{Q}(t) + Q(t) = K_p a_1 a_2 \ddot{E}(t) + K_p (a_1 + a_2) \dot{E}(t) + K_p E(t)$$

Second, discretize the equation:

$$b_1 b_2 \frac{(Q_{k+2} - Q_{k+1})}{\Delta t} - \frac{(Q_{k+1} - Q_k)}{\Delta t} + (b_1 + b_2) \frac{(Q_{k+1} - Q_k)}{\Delta t} + Q_k = K_p a_1 a_2 \frac{(E_{k+2} - E_{k+1})}{\Delta t} - \frac{(E_{k+1} - E_k)}{\Delta t} + K_p (a_1 + a_2) \frac{(E_{k+1} - E_k)}{\Delta t} + K_p E_k$$

Rearrange the equation, and it becomes:

$$\frac{b_1 b_2}{\Delta t^2} Q_{k+2} = -\left(1 - \frac{b_1 + b_2}{\Delta t} + \frac{b_1 b_2}{\Delta t^2}\right) Q_k - \left(\frac{b_1 + b_2}{\Delta t} - \frac{2b_1 b_2}{\Delta t^2}\right) Q_{k+1} + K_p \left(1 - \frac{a_1 + a_2}{\Delta t} + \frac{a_1 a_2}{\Delta t^2}\right) E_k + K_p \left(\frac{a_1 + a_2}{\Delta t} - \frac{2a_1 a_2}{\Delta t^2}\right) E_{k+1} + K_p \frac{a_1 a_2}{\Delta t^2} E_{k+2}$$

↓

$$Q_{k+2} = -\left(\frac{\Delta t^2}{b_1 b_2} - \frac{(b_1 + b_2)\Delta t}{b_1 b_2} + 1\right) Q_k - \left(\frac{(b_1 + b_2)\Delta t}{b_1 b_2} - 2\right) Q_{k+1} + K_p \left(\frac{\Delta t^2}{b_1 b_2} - \frac{(a_1 + a_2)\Delta t}{b_1 b_2} + \frac{a_1 a_2}{b_1 b_2}\right) E_k + K_p \left(\frac{(a_1 + a_2)\Delta t}{b_1 b_2} - \frac{2a_1 a_2}{b_1 b_2}\right) E_{k+1} + K_p \frac{a_1 a_2}{b_1 b_2} E_{k+2}$$

Finally, implement the above formula into LABVIEW, where a_1 , a_2 , b_1 , b_2 , and K_p are knowns, and Δt is the sampling time which equals to 0.5s.

3.2. Design of the feed-forward element

The controller was designed with assumption that there is no disturbance. In fact, the heat generation rate is a disturbance. When the heat generation rate is not equal to 0, there will be a large overshoot of the system, as shown in Figure 23.

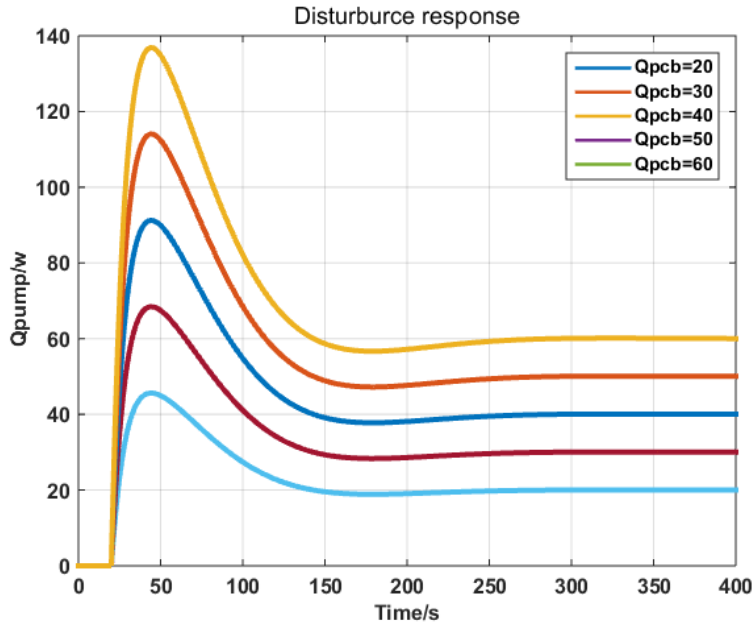


Figure 24: The response of the system when different disturbance applied

From the figure, we can see that the overshoot is more than 120% when the disturbance is applied to the system. In order to solve this issue, a feed-forward (FF) element is applied to minimize the overshoot of the response. The block diagram of an applied feed-forward element system is shown in Figure 25.

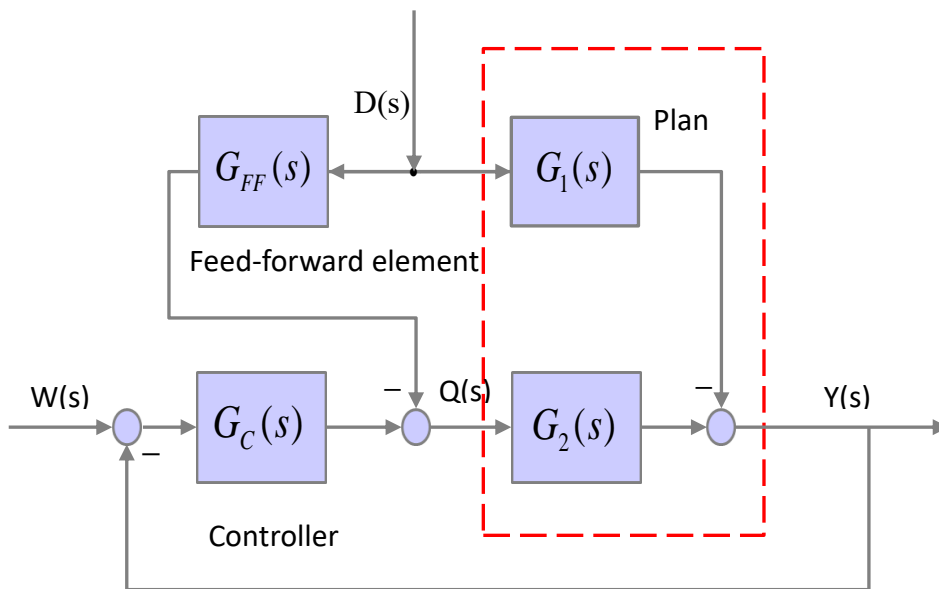


Figure 25: Block diagram of a system with feed-forward element

From the block diagram, we derive equation (3-9) and (3-10), where $D(s)$ is the disturbance .

$$Y = ((W - Y)G_C - DG_{FF})G_2 - DG_1, \quad (3-9)$$

$$Q = (W - Y)G_C - DG_{FF}, \quad (3-10)$$

Rearrange the equation (3-9), it becomes:

$$Y = WG_C G_2 - YG_C G_2 - DG_{FF} G_2 - DG_1,$$

$$Y = \frac{G_C G_2}{1 + G_C G_2} W - \frac{G_{FF} G_2}{1 + G_C G_2} D - \frac{G_1}{1 + G_C G_2} D,$$

(3-11)

$$Y = \frac{G_C G_2}{1 + G_C G_2} W - \frac{G_{FF} G_2 + G_1}{1 + G_C G_2} D,$$

Plug equation (3-11) into equation (3-10) and substitute Y, rearrange the equation, it becomes:

$$Q = G_C W - \frac{G_C G_2 G_C}{1 + G_2 G_C} W + \frac{G_{FF} G_2 G_C}{1 + G_2 G_C} D + \frac{G_1 G_C}{1 + G_2 G_C} D - G_{FF} D,$$

(3-12)

$$Q = \frac{G_C}{1 + G_C G_2} W + \frac{G_1 G_C - G_{FF}}{1 + G_C G_2} D$$

In order to eliminate the impact of the disturbance D on the output of the system Y, the term

$$\frac{G_{FF} G_2 + G_1}{1 + G_C G_2} D \equiv 0.$$

Then

$$G_{FF} = -\frac{G_1}{G_2}.$$

In this way, the disturbance can be compensated by the FF element, which is the basic idea.

However, the goal of our system is to make the output of the controller tracking the disturbance,

which means that Q should follow D. From the equation (3-12), we consider W is equal to 0, and it becomes:

$$\frac{Q(s)}{D(s)} = \frac{G_1 G_C - G_{FF}}{1 + G_C G_2}, \quad (3-13)$$

In ideal condition, Q follows D means

$$\frac{Q(s)}{D(s)} = 1,$$

then equation (3-13) becomes:

$$1 = \frac{G_1 G_C - G_{FF}}{1 + G_C G_2} \Rightarrow G_{FF} = G_C (G_1 - G_2) - 1.$$

Since the transfer function of G_1 , G_2 , and G_C have been determined in earlier chapter, G_{FF} can be determined. Applying G_{FF} to the system and simulating the system by using SIMULINK embedded in the MATLAB, the result is shown in Figure 26.

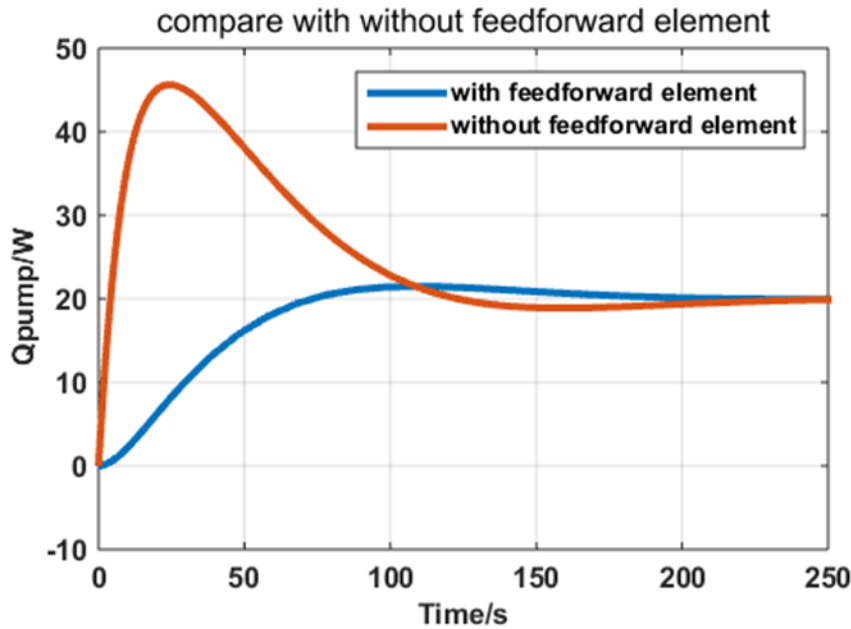


Figure 26: Comparison between the outputs of controller with/without FF element

Figure 26 shows that after applying feed-forward element, the settling time of the output of the controller do not change, but the overshoot reduces to less than 20%. The feed-forward element improve the performance of the system by reducing the overshoot by approximated 100%.

3.3. Design of Kalman Filter

3.3.1. Basic of Kalman Filter

Kalman filter was invented in 1960 by R. E. Kalman and is still widely used in control systems. It is a recursive dynamic estimator for what is called the linear-quadratic problem. The linear-quadratic method is used to estimate instantaneous states of a linear dynamic system perturbed by white noises. The resulting estimation is statistically optimal on any quadratic function of estimation errors [28].

Kalman filter is an estimator, can be also called an observer. In order to explain Kalman filter, an observer should be introduced first. A linear, time-invariant system in state space form can be written as follows:

$$\dot{\underline{x}} = \underline{A}\underline{x} + \underline{B}\underline{u} ,$$

$$\underline{y} = \underline{C}\underline{x} ,$$

where \underline{x} are the state variables that describe the dynamic and static behavior of the system given any set of inputs \underline{u} . \underline{y} is output and \underline{A} , \underline{B} and \underline{C} are the system matrices, and \underline{x} , \underline{y} and \underline{u} are all vectors.

In the linear systems, states of an unknown system can be tracked dynamically using a mathematical model that is similar to the unknown system. The difference between the outputs of the unknown system and the mathematical model product by the gain is the feedback to the mathematical model. As a result, errors of the states induced by different initial values between

the unknown system and the model can be compensated. Therefore, both of the states become likely identical. The mathematical model along with the gain is called an observer or estimator. It is defined that \hat{x} is the estimate states of the mathematical model, and an observer can be expressed in a state space form as:

$$\dot{\hat{x}} = \underline{A}\hat{x} + \underline{B}u + \underline{L}(y - \underline{C} \cdot \hat{x}) .$$

The following diagram shows an observer.

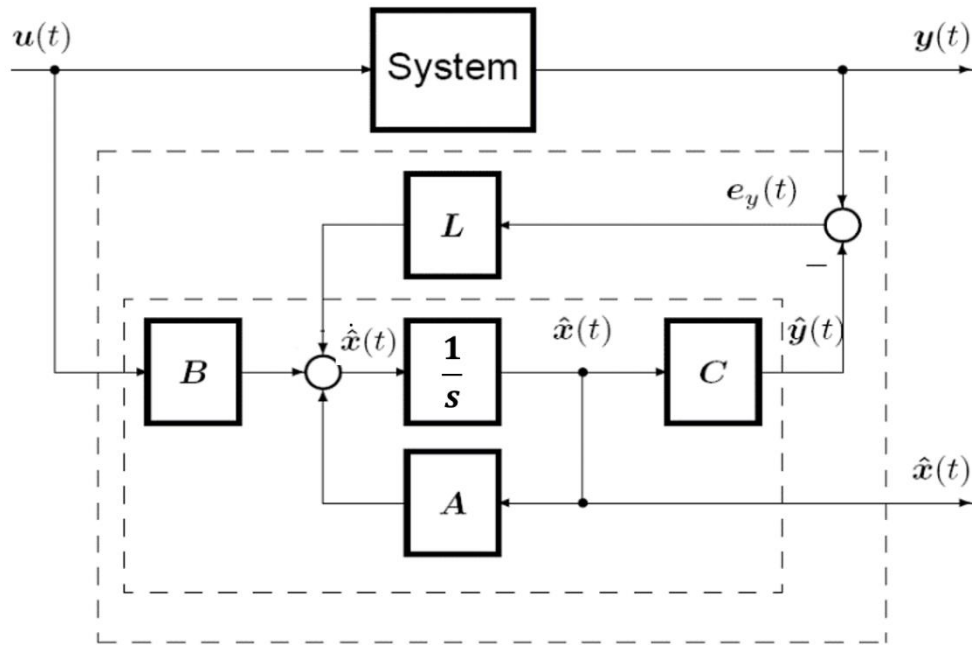


Figure 27:Block diagram of observer

The estimation error is defined as: $\tilde{x} = x - \hat{x}$ that can be vanished by choosing a proper gain

L. The dynamics of estimation error is described as:

$$\begin{aligned} \dot{\tilde{x}} &= \dot{x} - \dot{\hat{x}} \\ &= \underline{A}x + \underline{B}u - [\underline{A}\hat{x} + \underline{B}u + \underline{L}(y - \underline{C} \cdot \hat{x})] \\ &= \underline{A}(x - \hat{x}) - \underline{L}(\underline{C}x - \underline{C}\hat{x}) \\ &= (\underline{A} - \underline{L}\underline{C})\tilde{x} \end{aligned} \tag{3-14}$$

From equation (3-14), the error dynamics are stable if eigenvalues of (A-LC) are in the left half of the complex plane. If and only if the system is observable, the eigenvalue of (A-LC) can be freely chosen.

In general, a system is called observable when the current states can be determined by the outputs (usually by measuring) in a finite time. The observability matrix of a system can be expressed as:

$$\underline{V}_n = \begin{bmatrix} \underline{C} \\ \underline{CA} \\ \vdots \\ \underline{CA}^{n-1} \end{bmatrix}$$

When \underline{V}_n is in full rank, the system is observable.

Therefore, the estimation error can be compensated by a proper selection of the gain (L). Kalman filter is an algorithm that can calculate the gain and update it during processing. It can be said that Kalman filter is an estimator that the gain is automatically changing based on the input of the system.

3.3.2. Implementation of Kalman Filter

The discrete model used for Kalman filter is a linear system with stochastic noises, which the equation expresses as follows:

$$x_k = Ax_{k-1} + Bu_k + w_k \tag{3-15}$$

With a measurement equation:

$$z_k = H \cdot x_k + v_k \tag{3-16}$$

The variables w_k and v_k are process and measurement noises, respectively. We assume that they are Gaussian white noises and not correlate with each other. It is satisfied a normally distributed probability as follows:

$$p(w) \sim N(0, Q),$$

$$p(v) \sim N(0, R).$$

There are plenty of published documents that explain how Kalman filter works. In this study, the core part of Kalman filter is summarized by five equations. A linear state space model is defined as:

$$x_k = Ax_{k-1} + Bu_k + w_k,$$

$$z_k = H \cdot x_k + v_k,$$

Priori predicted state update:

$$\hat{x}_k^- = A\hat{x}_{k-1} + Bu_k \quad 1.$$

Priori prediction error covariance update:

$$P_k^- = AP_{k-1}A^T + Q \quad 2.$$

Kalman gain update:

$$K_k = (P_k^- H^T)(HP_k^- H^T + R_k)^{-1} \quad 3.$$

Posterior estimated state update:

$$\hat{x}_k = A\hat{x}_k^- + K(z_k - H\hat{x}_k^-) \quad 4.$$

Posterior estimation error covariance update:

$$P_k = (I - K_k H)P_k^- \quad 5.$$

Where k= 1, 2, 3 ...

1 and 2 are the time update equations; 3, 4 and 5 are the measurement update equations. Initial values of the prior predicted and the posterior estimated states should be provided at first and initial value of error covariance is 0.

Recall the mathematical model of the metal plate that is studied in Chapter 2:

$$T_1^{k+1} = \frac{\Delta t}{C_M m_M} Q_{PCB}^k + \left(1 - \frac{\Delta t K}{C_M m_M}\right) T_1^k + \frac{\Delta t K}{C_M m_M} T_2^k \quad (2-23a)$$

$$T_2^{k+1} = -\frac{\Delta t}{C_M m_M} Q_{pump}^k + \left(1 - \frac{\Delta t K}{C_M m_M}\right) T_2^k + \frac{\Delta t K}{C_M m_M} T_1^k \quad (2-23b)$$

We assume that Q_{PCB}^k is a constant during the sampling time and

$$Q_{pump}^k = k_1 T_2^k I_{TEM}^k - k_2 I_{TEM}^k{}^2 - k_3 (T_3^k - T_2^k), T_2^k = 2T_{initial}^k - T_1^k$$

Therefore, the above equations are rewritten as:

$$\begin{bmatrix} T_1^{k+1} \\ T_2^{k+1} \\ Q_{PCB}^{k+1} \end{bmatrix} = \begin{bmatrix} 1 - \frac{K\Delta t}{C_M m_M} & \frac{K\Delta t}{C_M m_M} & \frac{K\Delta t}{C_M m_M} \\ \frac{K\Delta t}{C_M m_M} & 1 - \frac{K\Delta t + k_3}{C_M m_M} & 0 \\ 0 & 0 & 1 \end{bmatrix} \begin{bmatrix} T_1^k \\ T_2^k \\ Q_{PCB}^k \end{bmatrix} + a^k \begin{bmatrix} 0 \\ -\Delta t \\ 0 \end{bmatrix} I_{TEM}^k$$

$$+ \begin{bmatrix} 0 \\ \frac{k_2 \Delta t}{C_M m_M} \\ 0 \end{bmatrix} (I_{TEM}^k)^2 + \begin{bmatrix} 0 \\ \frac{k_3 \Delta t}{C_M m_M} \\ 0 \end{bmatrix} T_3^k$$

$$y^k = \begin{bmatrix} 1 & 0 & 0 \end{bmatrix} \begin{bmatrix} T_1^k \\ T_2^k \\ Q_{PCB}^k \end{bmatrix}$$

, where $a^k = k_1(2T_{initial}^k - T_1^k)$. T_1 , T_3 , and I_{TEM} are measured directly, and they are the inputs of the Kalman filter. Then the diagonal values of process covariance are selected as 10^{-3} , 10^{-3} , and 10^{-2} ; the diagonal values of measurement covariance are selected as 10^{-2} , 10^{-2} and 10^{-2} .

3.4. Simulation

Before doing the experiment, the whole process is simulated using SIMULINK, the block diagram of the simulation is shown as follows:

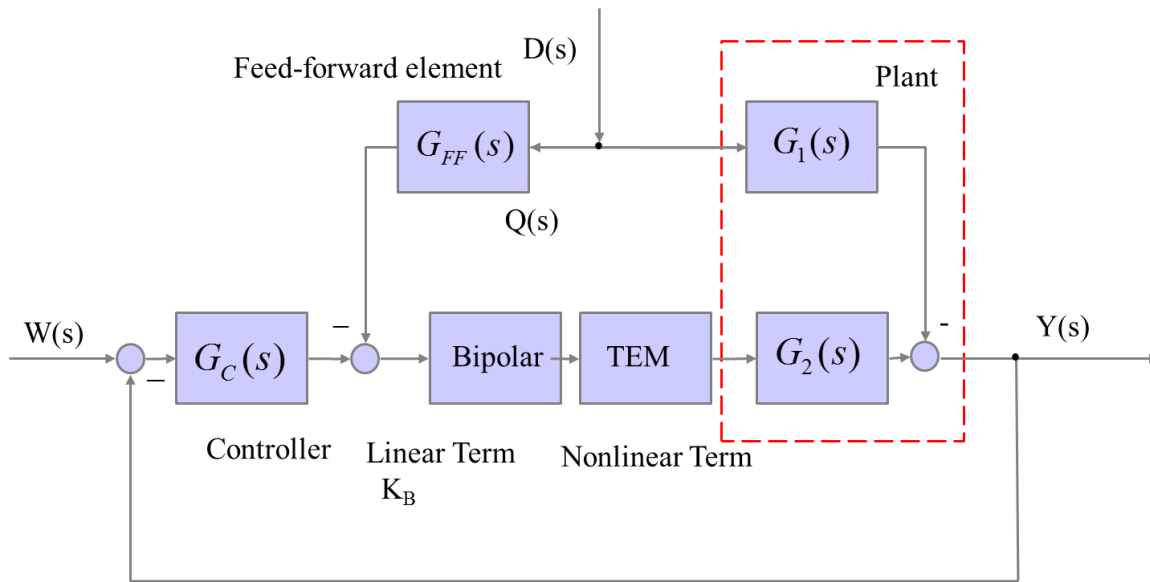


Figure 28: The block diagram of the calorimeter system

The controller is a lead-lag compensator that is designed in previous chapter. The compensator and the feed-forward element are embedded in LABVIEW, the amplifier is the module (SCC-FT01) from NI. The output of the module is a voltage signal that controls the bipolar power supply, which the output produces a current that applied to the TEM, the outputs of the bipolar power supply have a linear relationship with the inputs: output (current) = 1.5 * input (voltage). The TEM has a nonlinear relationship between its input (current) and its output (heat pump rate) which is discussed in chapter 2.

In order to simplify the simulation, we hope the heat pump rate of the TEM is only determined by the current applied to it. Recall the equation from chapter 2:

$$Q_{pump} = k_1 T_2 I_{TEM} - k_2 I_{TEM}^2 - k_3 (T_3 - T_2).$$

The first term represents the heat pump rate, the second term represents the heat generation rate and the third term represents the heat conduction rate of the calorimeter. From the experiment data, we can see that T_2 varies within 6K, and T_3 is the ambient temperature varying between 0.2K. Therefore, we assumed that the coefficient of the heat pump rate is constant. The second and the third term: heat generation and heat conduction, which decrease the efficiency of the calorimeter are combined into one term. The above equation becomes:

$$Q_{pump} = a \cdot I_{TEM} - b \cdot I_{TEM}^2.$$

Using the least squares method, $a=41.89$; $b=-4.566$ are obtained, shown as follows:

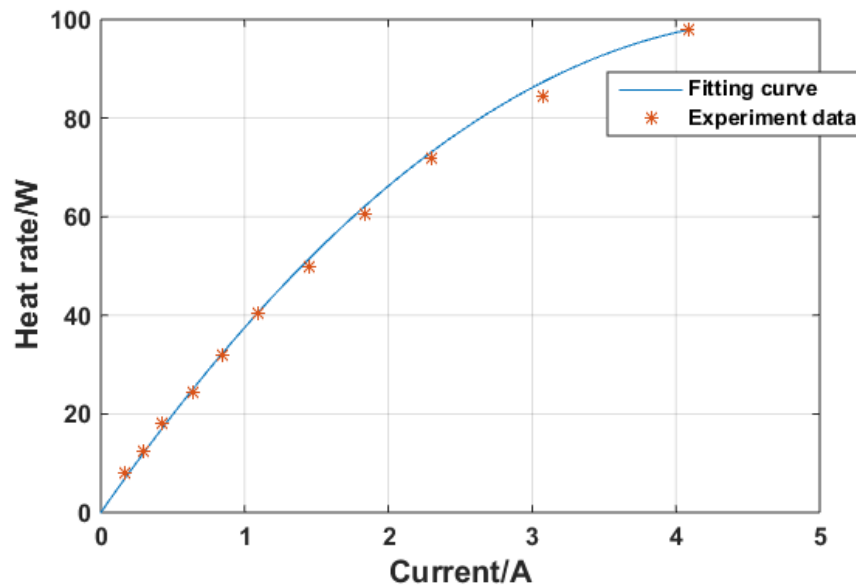


Figure 29: Comparison between the fitting curve and experiment data

The block diagram using SIMULINK is shown in Figure 30. It simulates that when a step heat generation applied to the metal plate, the compensator will give a voltage signal to the bipolar

power supply, and then the bipolar power supply gives a certain current to the calorimeter. The calorimeter will generate a heat pump rate applied to the metal plate. The temperature profile of the metal plate in TEM side and PCB side are recorded as well as the current applied to the TEM.

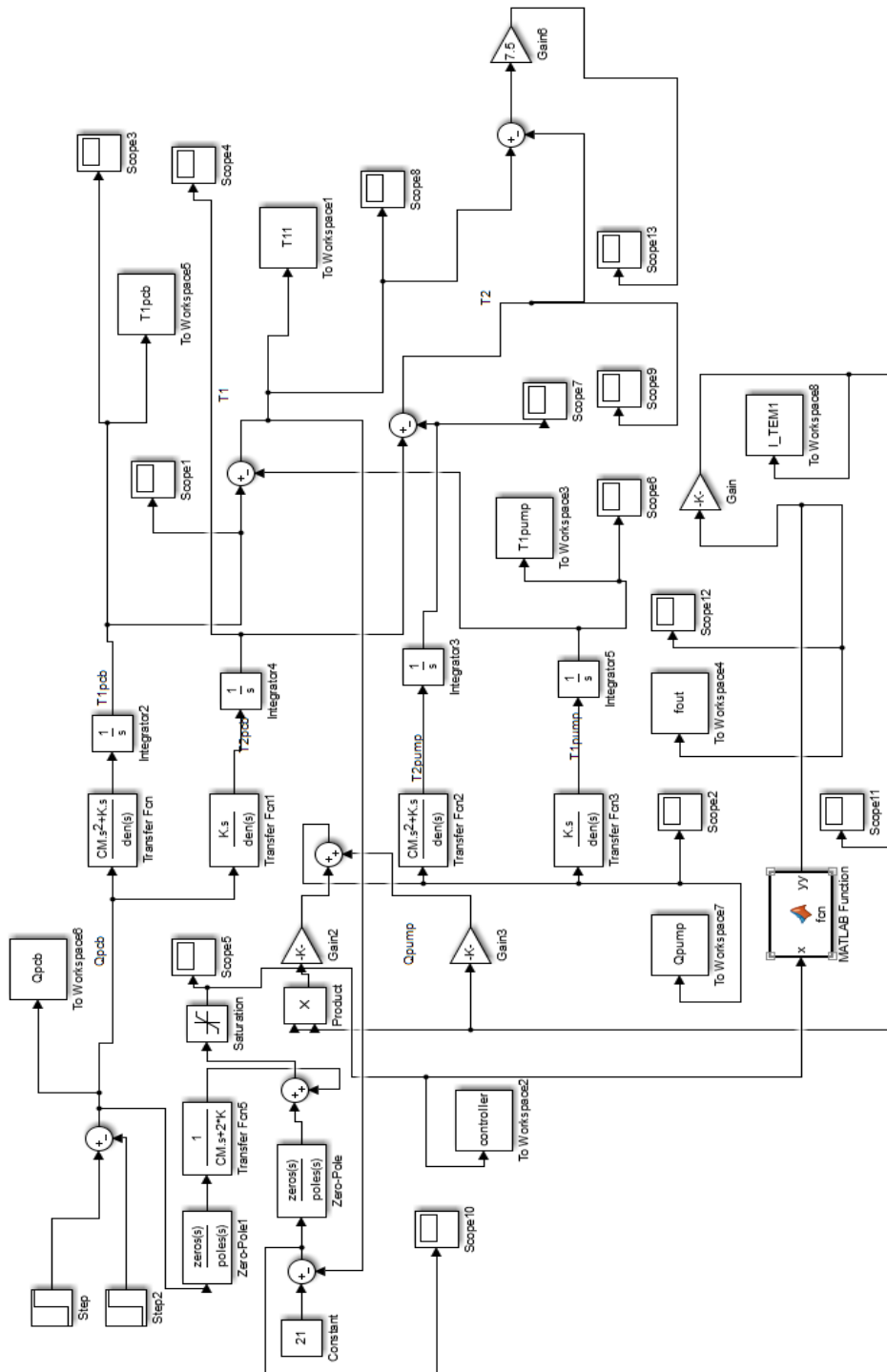


Figure 30: Block diagram of the calorimeter

In the simulation, we first apply a 60W heat generation rate as a disturbance to the calorimeter system, which simulates the heat generation by the PCB. The ambient temperature in the test environment is $21\pm 0.2^{\circ}\text{C}$. Therefore, the initial value of the metal plate temperature is set to be 21°C . The temperature response of the metal plate in the PCB side is shown in Figure 31

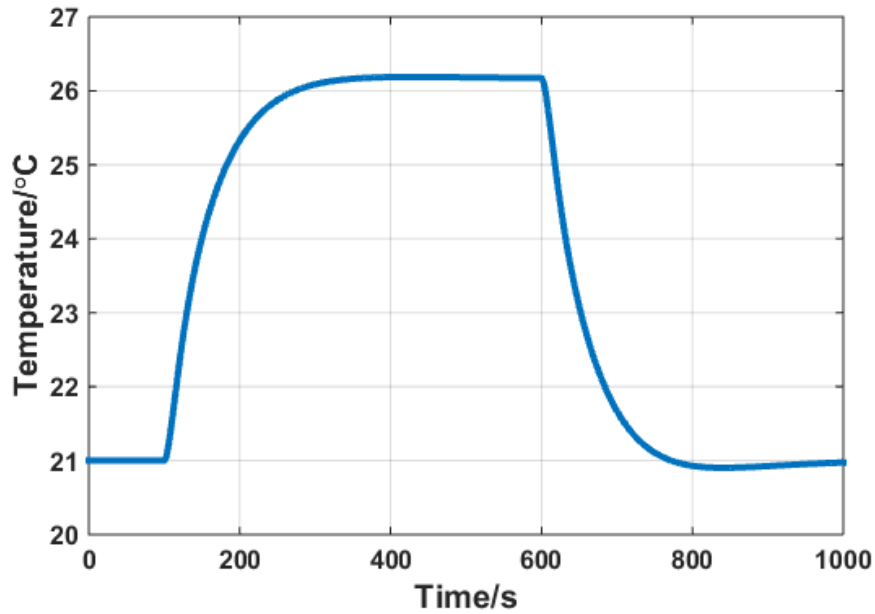
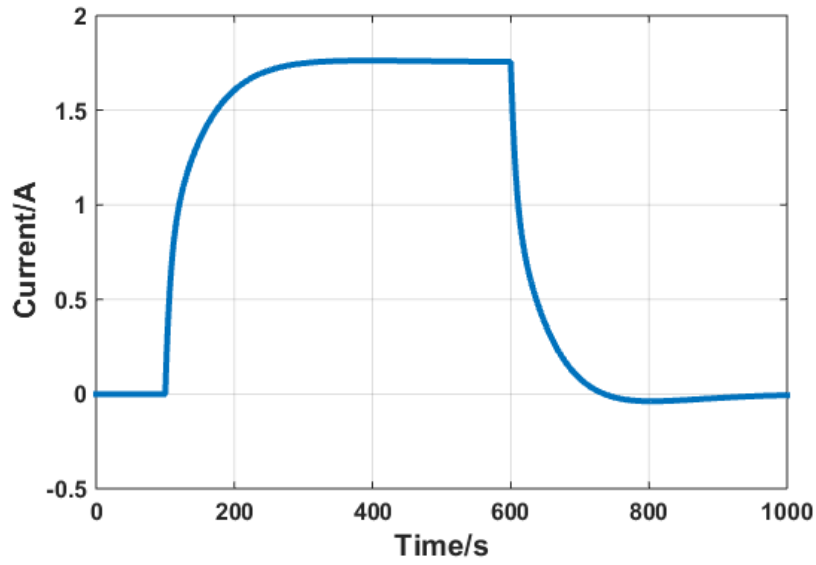


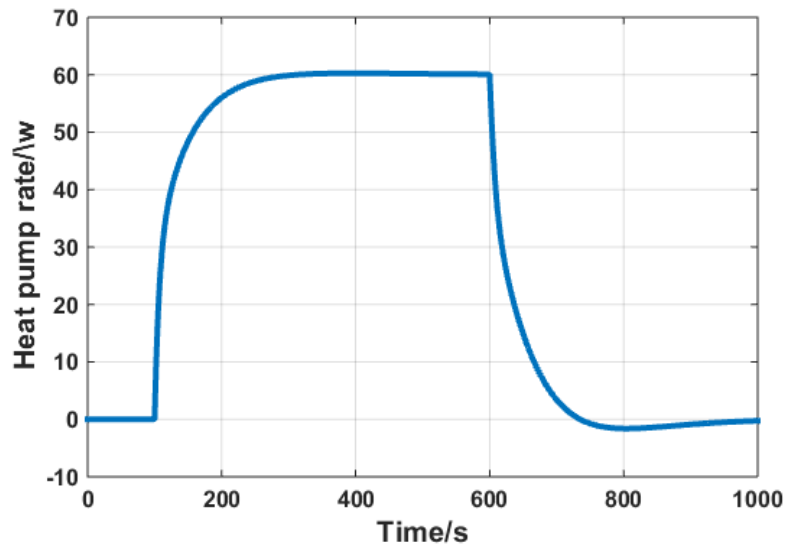
Figure 31: Temperature of the metal plate in PCB side

From the figure, we can find that the temperature rises from 21°C to 26.2°C in 200 seconds and enters into the steady state. When the disturbance is removed at the 600 seconds, the temperature drops to 21°C , which means that the total heat generated by the PCB is the same as the total heat pump by the TEMs.

Figure 32 (a) shows the current applied to the calorimeter controlled by the designed compensator.



(a)

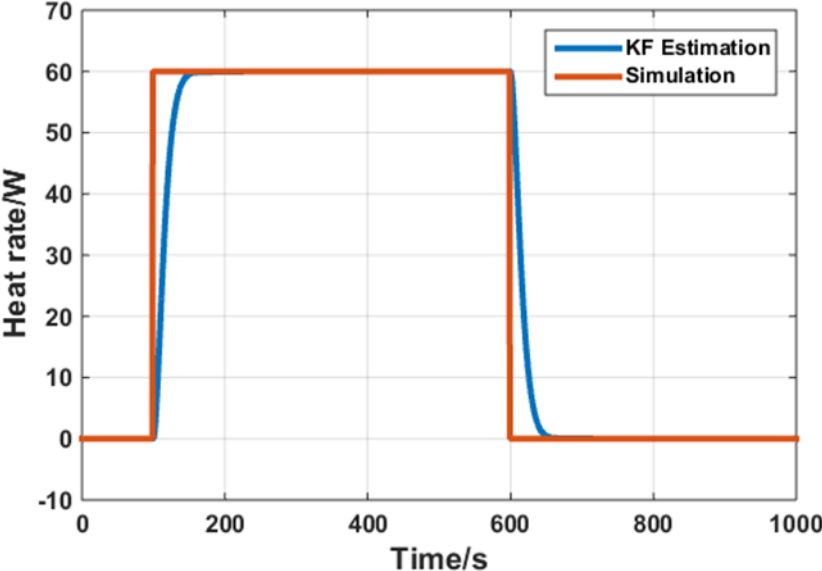


(b)

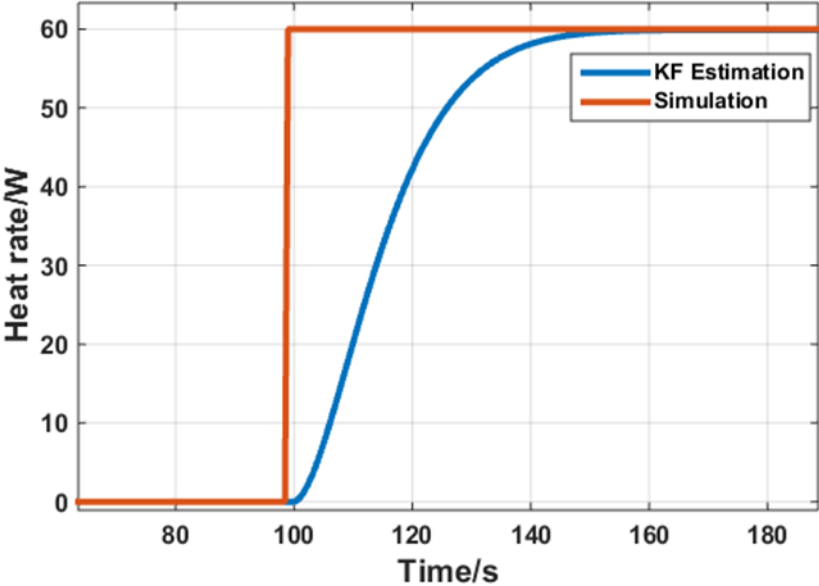
Figure 32: (a) The current applied to the calorimeter (b) Estimated heat generation rate of the calorimeter

The two figures show the compensator controls the current that is applied to the calorimeter precisely, and the heat pump rate generated by the calorimeter follows the disturbance in 150 seconds without any overshoot. The temperature profile and the current profile shown in Figure

32 (a), (b), respectively, that are the input of Kalman filter. The estimated heat generation rate of the PCB by Kalman filter is shown in Figure 33.



(a)



(b)

Figure 33: (a) Comparison between the estimation result and the simulation result (b) Zoomed-in dynamic response

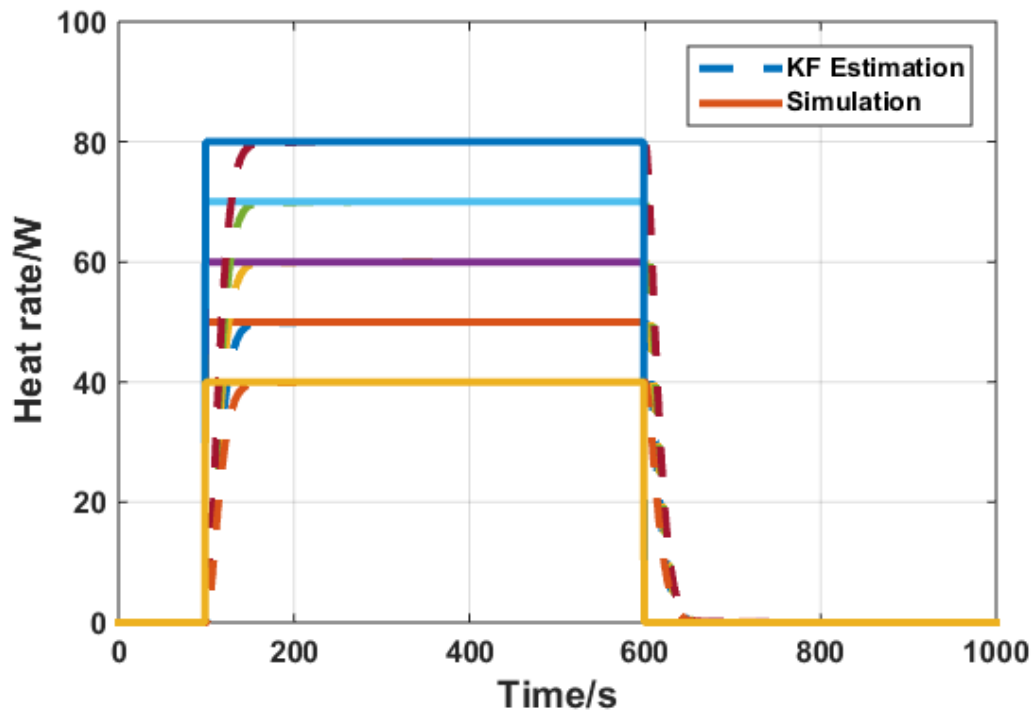


Figure 34: Estimated results by Kalman filter

Figure 33 (b) shows that the estimated heat generation rate by Kalman filter is exactly 60W and it takes 50 seconds to converge. Five simulation runs are made, and the results are shown in Figure 34. The heat generation rate is estimated accurately within 50 seconds.

4. Heat generation measurement

4.1. Measurement of the PCB heat generation

Before testing the battery, the heat generation rate for a PCB is measured. Since the heat generation rate of the PCB can be easily calculated with the applied current, and the heat generation rate can be assumed to be constant during the test period, the steady state behavior of the calorimeter can be tested accurately.

The PCB has the same size as that of the battery and which resistance is 0.499Ω . After mounted, different values of the step current are applied to generate a step form of the heat generation rate. At the same time, a current controlled by the compensator is applied to the calorimeter to pump out the heat in order to keep the average temperature of the metal plate constant. The current controlled by the compensator that applied to the calorimeter when the PCB's heat generation rate is 10W, 20W, 30W, 40W, 50W respectively is shown in Figure 34.

Before the cycle starts, there is an 1800 seconds preparation, and during this period, the calorimeter and the PCB are at rest. Then the PCB produced a step of 10W heat generation rate for 1800 seconds and rested for another 1800 seconds. At the same time, the compensator generates a certain current to the calorimeter. The calorimeter works as a heat pumper to maintain the average temperature of the metal plate same as the ambient temperature. Five cycles were tested and each cycle has a different heat generation rate of the PCB.

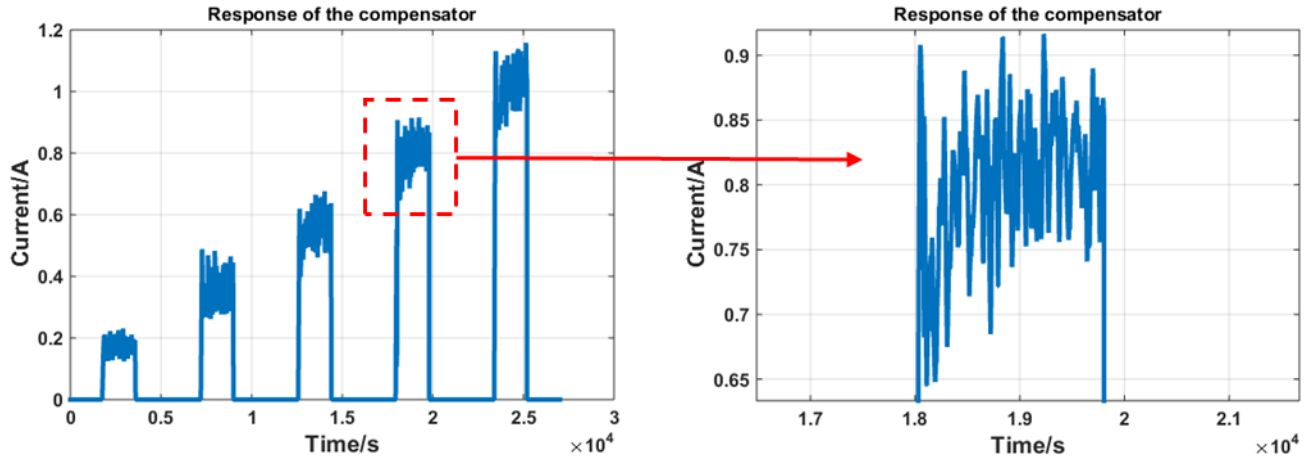


Figure 35: Current applied to the calorimeter

The Figure 35 shows that in the steady state, with the heat generation rate of the PCB increasing, the current that is controlled by the compensator in the steady state increasing at the same time. $\pm 0.15\text{A}$ varies in the steady state caused by noises. According to the equation

$$Q_{pump} = k_1 T_2 I_{TEM} - k_2 I_{TEM}^2 - k_3 (T_3 - T_2),$$

$k_1, k_2,$ and k_3 are determined in chapter 2. I_{TEM} and T_1, T_3 and T_{amb} can be measured directly. $T_2 = 2T_{initial} - T_{working}$. Therefore, heat pump rate of the calorimeter can be calculated and is shown in Figure 35.

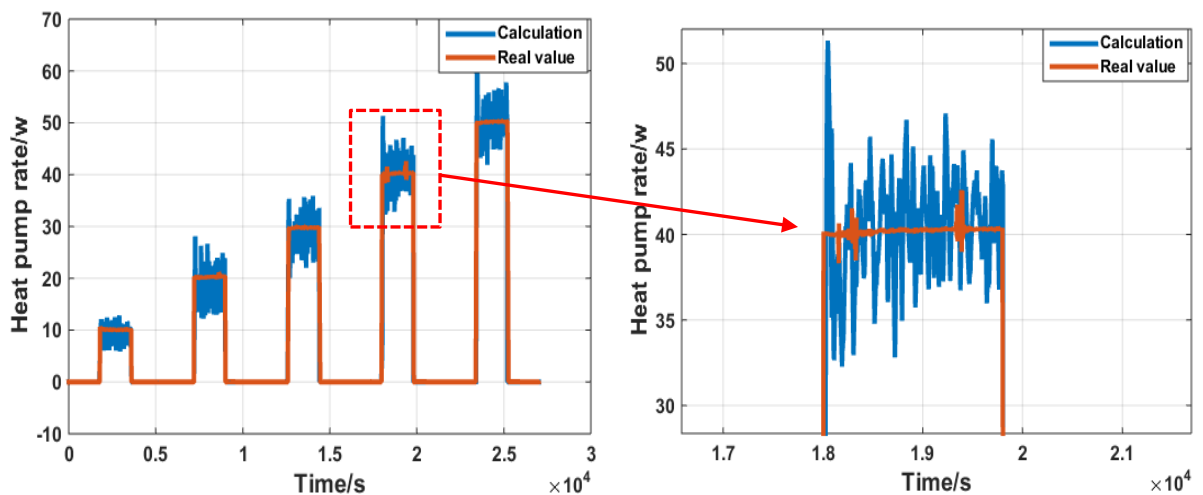


Figure 36: Comparison between the calculated and real heat generation rate

Figure 36 shows a large steady state error (about 5W) from the calculation due to noises. In order to solve this problem, a Kalman filter is used and the results are shown below.

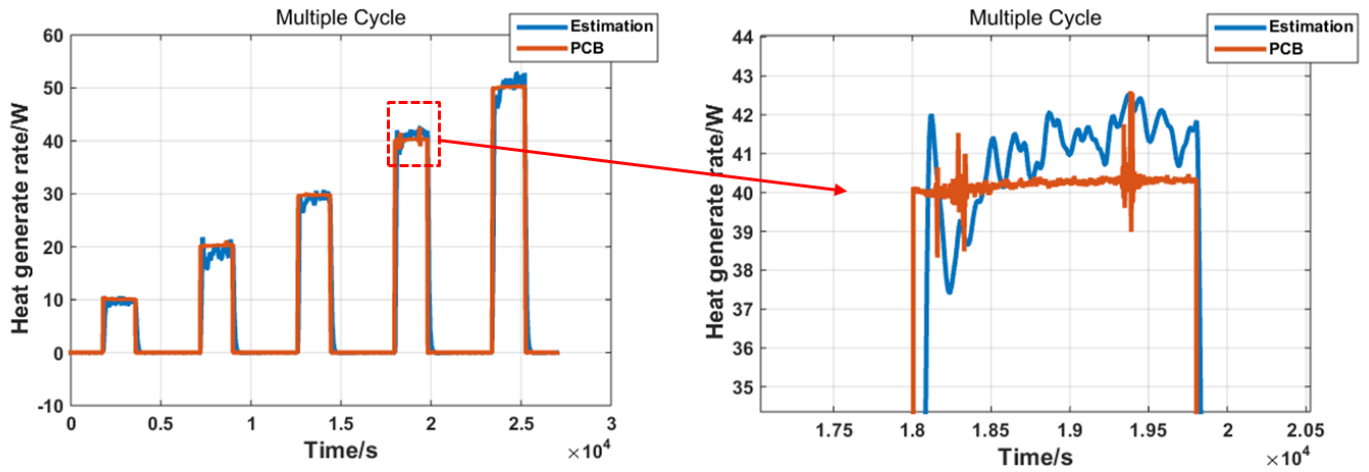


Figure 37: Static performance of Kalman filter estimation

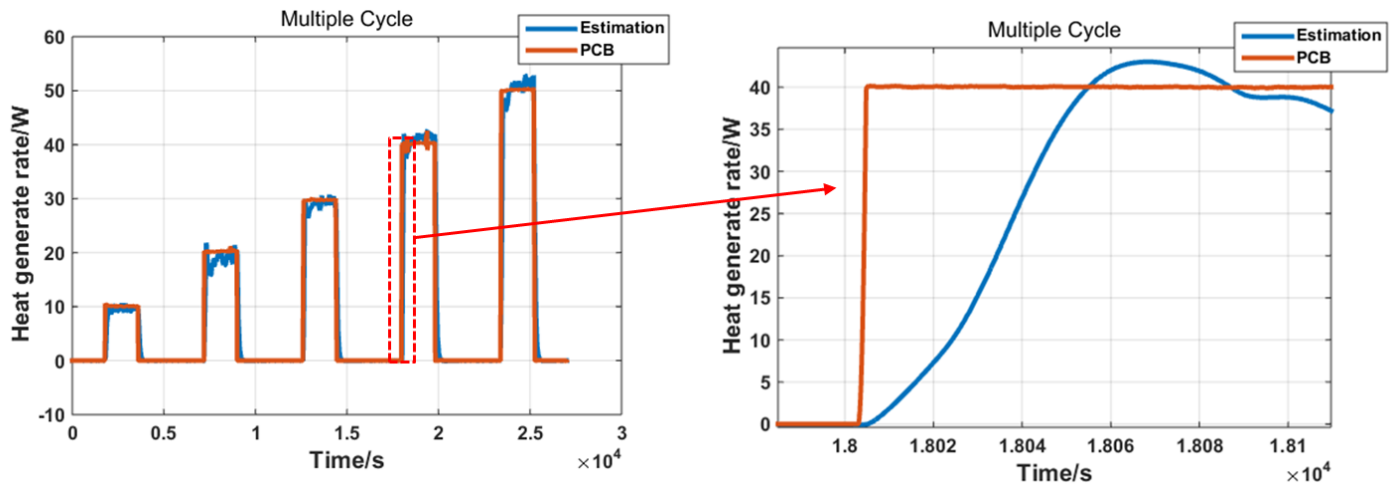


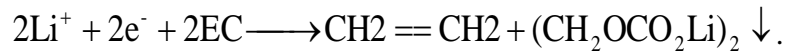
Figure 38: Dynamic performance of Kalman filter estimation

After applying the Kalman filter, both the static and dynamic response of the heat generation rate estimation of the PCB are improved. The steady error becomes less than 5%, and it takes about 60 seconds to follow the measured heat generation rate. Figure 37 and Figure 38 shows the static and dynamic behavior of the applied KF.

4.2. Measurement of heat generation rate of lithium-ion pouch battery

4.2.1. Solid electrolyte interphase (SEI)

Before testing a fresh lithium ion battery, ‘initial cycles’ must be done, which means the battery needs to be discharged to 0% SOC and charged to 100% SOC with 1C rate for five times. Solid electrolyte interphase (SEI) is a thin layer that adheres to the surface of the anode particles. It is the product of the side reactions that take place on the anode side. The two main side reactions are [29]:



During charging and discharging of the battery, the side reactions continue to take place, and the chemical products will accumulate, and cause the increase in the SEI thickness. Once a SEI is formed, it can prevent lithium ions having a chemical reaction with the solvents of the electrolyte, therefore, protecting the active material of the lithium-ion battery. However, with SEI growing, the ionic resistance of the electrodes continues to increase and lead to power fade, moreover, SEI prevent the lithium-ion to the electrodes leading to capacity fade [29].

During the initial cycles, the calorimeter works as a thermal isolator that maintains the surface temperature of the battery at 25°C. Heat generation of the battery with 1C charge or discharge is relative small, the surface temperature cannot reach to 25°C under the condition that the ambient temperature is 22.5°C. Therefore, the calorimeter needs to generate heat instead of pumping heat. The characteristic of a TEM has been already discussed in chapter 2, changing the direction of the current can change the hot side and the cold side of the calorimeter. Then a PI controller is used to control the calorimeter that makes it generating heat to maintain the surface

temperature at 25°C. The parameters of the PI controller is tuned manually online. Maintaining the temperature is another advantage of the designed calorimeter since it acts as a battery surface temperature keeper, not only as a heat generation rate observer. The following figures show the surface temperature of the battery during rest and charging/discharging mode.

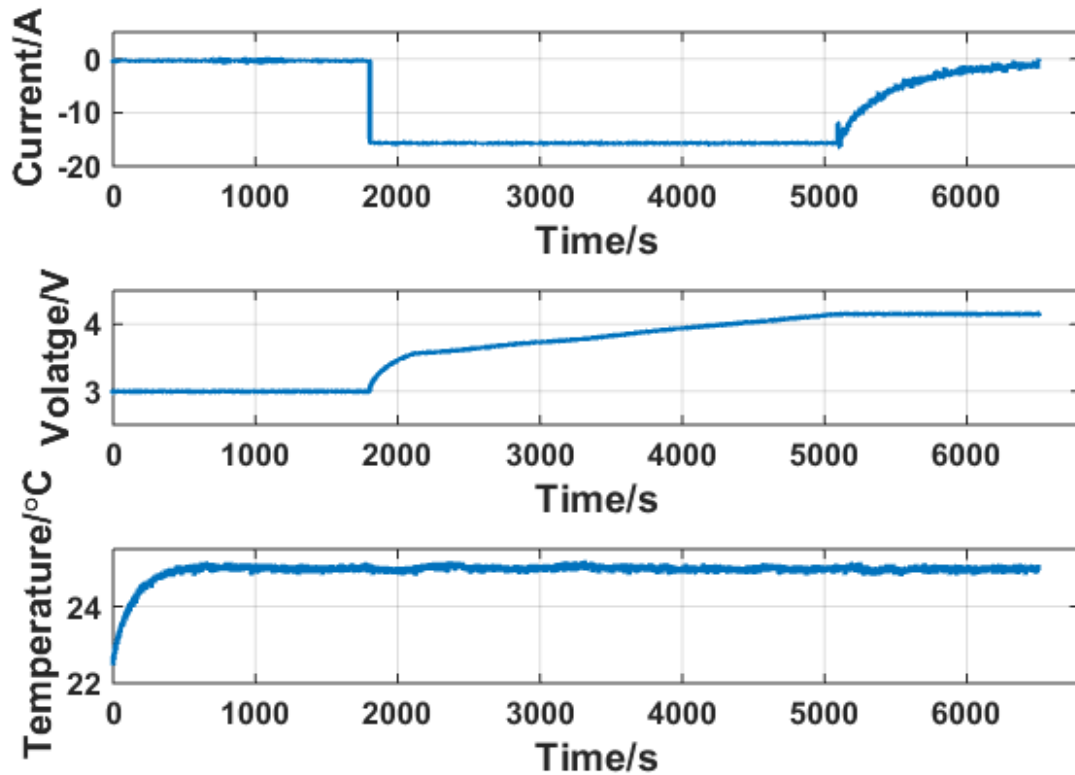


Figure 39: An initial cycle in charge model

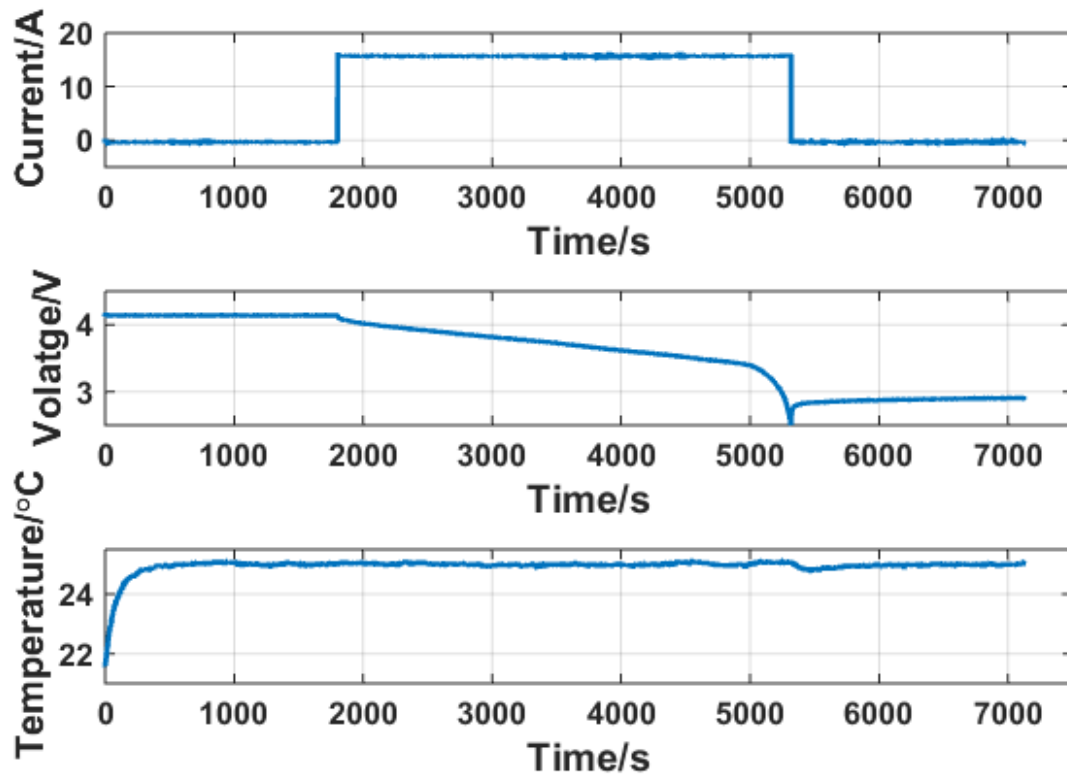


Figure 40: An initial cycle in discharge model

The two figures show that the initial temperature of the battery surface is the same as the ambient temperature. The designed calorimeter heats up the battery surface to 25°C in 250 seconds. No matter the battery in rest, charge or discharge mode, the surface temperature of the battery is always kept at 25°C.

4.2.2. Heat generation

The total heat generation by a Li-ion battery (Q_{tot}) can be defined as two heat sources: reversible (Q_{rev}) and irreversible heat (Q_{irr}).

$$Q_{tot} = Q_{rev} + Q_{irr} .$$

The governing equation of reversible heat generation is expressed as:

(4-1)

$$Q_{rev} = -I \cdot T \cdot \frac{\partial V_{OCV}}{\partial T},$$

where I is the charging or discharging current and the sign is negative when charging. T is the temperature inside of the battery and V_{OCV} is the open circuit voltage (OCV). From equation (4-1), a lithium ion battery absorbs heat when it is charged and releases heat when it is discharged. In the chemical reaction, this term is the change of entropy expressed as (ΔTS).

In general, there are two main methods to estimate irreversible heat generation of a lithium ion battery. The first one is calculated by the following equations [2] [11] [16]:

$$\begin{aligned} Q_{irr} &= Q_{reaction} + Q_{ohm} \\ Q_{reaction} &= \int I \cdot (\phi_1 - \phi_2 - U_{equ}) \cdot dV \\ Q_{ohm} &= \int [\sigma^{eff} (\nabla \phi_1)^2 + (\kappa^{eff} \cdot \nabla \phi_2 + \kappa_D^{eff} \nabla \ln c_e) \cdot \nabla \phi_2] \cdot dV \end{aligned}$$

, where I is the current. The current flowing from the electrode to the electrolyte is defined as positive. ϕ_1 is the electrode potential, ϕ_2 is the electrolyte potential, U_{equ} is the equilibrium potential. σ^{eff} is the effective conductivity in the electrode. κ^{eff} and κ_D^{eff} are the effective conductivity in the electrolyte and the effective diffusion conductivity in the electrolyte respectively. c_e is the concentration of the electrolyte. The second method is expressed by the equation (4-2):

(4-2)

$$Q_{irr} = I \cdot (V_{OCV} - V_t),$$

where I is charge/discharge current. V_{OCV} is the open circuit voltage. V_t is the terminal voltage. This formula describes the irreversible heat generation caused by the product of the voltage drop and the current. It assumes that when a lithium ion battery is charging or discharging, there is a voltage difference between the terminal voltage and the open circuit voltage due to ion and electron

transport and chemical reactions that take place inside of the battery. However, according to equation (4-2), irreversible heat generation becomes zero when the current is zero, therefore, the heat of mixing is not considered in this equation. In reality, the irreversible heat is continuously generated due to non-uniform distribution of the electrochemical energy that is denoted as the heat of mixing [2].

In summary, the first method is complicated, and the parameters are hard to obtain. In addition, this equation does not consider the enthalpy heating that cannot neglect in this study [2]. Therefore, we cannot use the method to calculate irreversible heat generation. In contrast, the second method is easy to calculate because I and V_t can be measured directly, and V_{OCV} is a function of SOC. Then using the coulomb counting method to calculate SOC, find the function $V_{OCV}=f(SOC)$. For reversible heat, the current can be measured directly, and we assume that surface temperature of the battery is the same as the temperature inside of the battery, so that it can be measured directly too. Some researchers have tested the same type of the battery, and denoted that $\partial V_{OCV}/\partial T$ is a constant, equals to 2.2×10^{-4} V/K [2]. So far, we can estimate reversible heat. In reality, the reversible heat is significant at low charging/discharging rates, however, in this study, the aim of the experiments are a preparation for fast charging which means a high current (more than 4C) is needed for the battery. Therefore, the reversible heat is relatively small compare with the irreversible heat in our experiments. For the heat of mixing term, it is also relatively small compares to irreversible heat and can be neglected during charging or discharging of the battery. When the current is cut off, there is a period that ion concentrations are not uniformly distributed inside of battery and vanish until the concentration gradient does not exist. It can be described as [30]:

$$Q_{mixing} = \int \sum_j \sum_i (\overline{H_{ij}} - \overline{H_{ij}^{avg}}) \frac{\partial c_{ij}}{\partial t} dv,$$

where $\overline{H_{ij}}$ is the partial molar enthalpy of particles i in phase j . $\overline{H_{ij}^{avg}}$ is average partial molar enthalpy of particles i in phase j . c_{ij} is the concentration of particles i in phase j . dv is the differential control volume. This kind of heat becomes the only heat source term after the current is cut off. However, an electrochemical model of the battery needs to be established to estimate the heat of mixing. We do not have the model in this study and neglect this term in the theoretical calculation.

4.2.3. Open circuit voltage (OCV) and SOC

Open circuit voltage is the difference of the equilibrium potentials of both electrodes. It can be measured directly when the battery is not loaded.

The SOC is defined as the ratio between the energy that the battery can release ($Q_{releasable}$) and the maximum capacity (Q_{max}) of the battery.

$$SOC = \frac{Q_{releasable}}{Q_{max}} \times 100\% ,$$

where $Q_{releasable}$ and Q_{max} have a unit of ampere-hour (Ah). SOC is also expressed by the following equation:

$$SOC = SOC_0 + \int I(t)dt, \tag{4-3}$$

where SOC_0 is the initial value, and I is the terminal current, which sign is defined as positive when charged.

In order to find the relationship between OCV and SOC, a fresh battery should be fully charged at the first. Under this condition, SOC of the battery is 100%. Then a discharging pulse

current is applied to the battery, the response of the terminal voltage is measured until the battery is fully discharged. The discharging rates and the pulse duration is dependent upon the battery types. After each pulse, the battery should have enough time to rest. At this time, the terminal voltage is the OCV of the battery and SOC can be calculated from equation (4-3) as well. Therefore, OCV is a stoichiometry function with SOC, which is a nonlinear function. The nonlinear relationship is approximated by two exponential functions:

$$OCV = a \cdot e^{b \cdot SOC} + c \cdot e^{d \cdot SOC} .$$

For the test battery in this thesis, $a=3.418$, $b=0.001902$, $c=0.8846$, $d=0.2759$.

The following figure shows the relationship between SOC and OCV. Both experimental data and the fitting curve are compared in this figure.

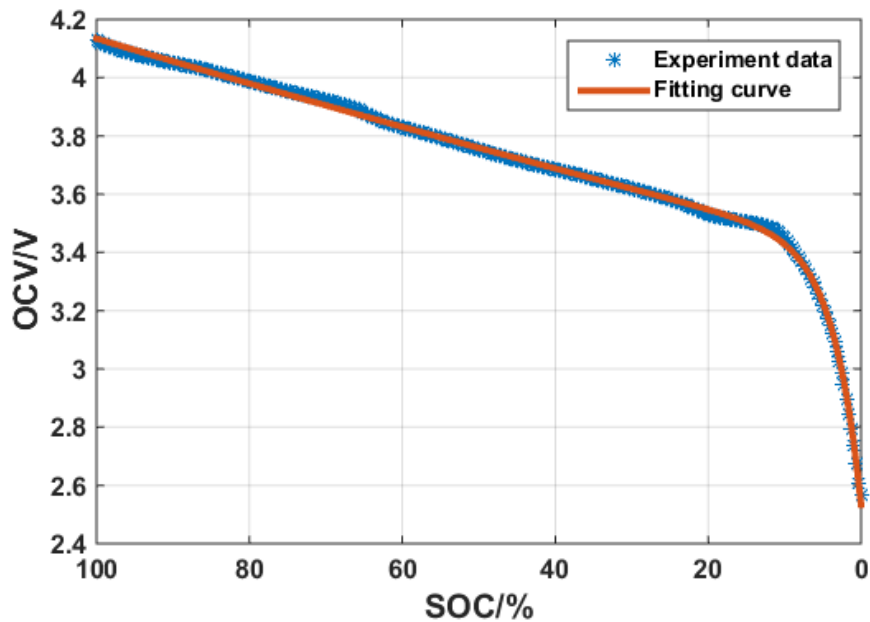


Figure 41: SOC-OCV curve

4.3. Experiment

In this study, a high current (up to 95A) is applied to the battery so that a large heat generation occurs at the clamps and the terminal taps of the battery. In order to minimize the contact resistance

between the clamps and the terminal taps of the battery, a 300lbs force is applied on them, and the clamps are made of copper that cover the whole area of the taps. When a 95A (6C) charging current is applied to the battery, the temperature measured at the clamp is shown as follow:

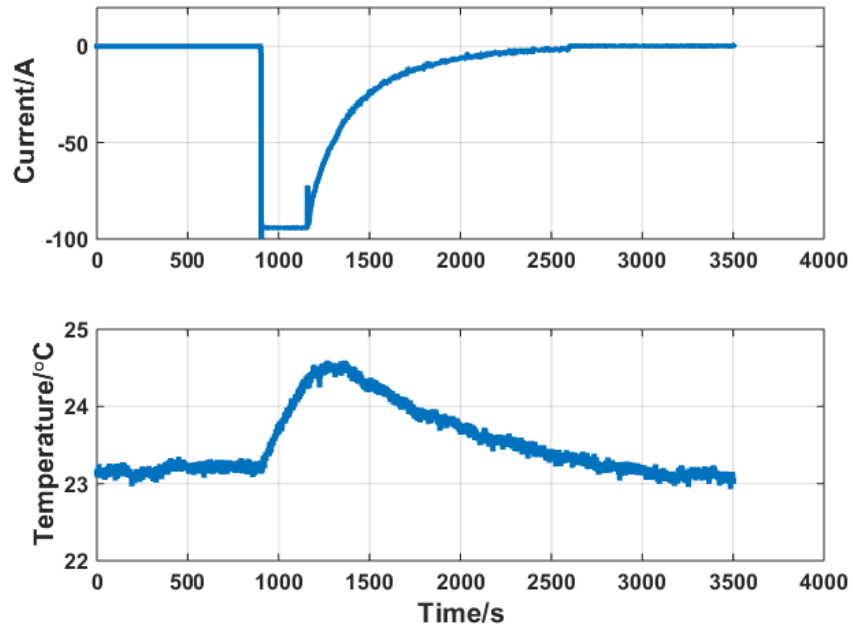


Figure 42: Temperature of the clamp

It shows that the temperature of the clamp only rises 1.5°C so that the effects of the contact resistance and the heat generation at the clamps can be excluded.

The total heat generation of the battery is measured when the battery is discharging at different currents in the constant current (CC) mode. When the battery is charging at different currents, it charges in the CC mode at first, when the terminal voltage reached 4.15V, it charges with constant voltage (CV) to make sure that the battery is fully charged. Experiment results and the calculation results (based on equation 4-1 and 4-2) are shown in Figure 42. The solid lines and the dash lines represent experimental data and calculation results. The calculation results do not consider the heat of mixing.

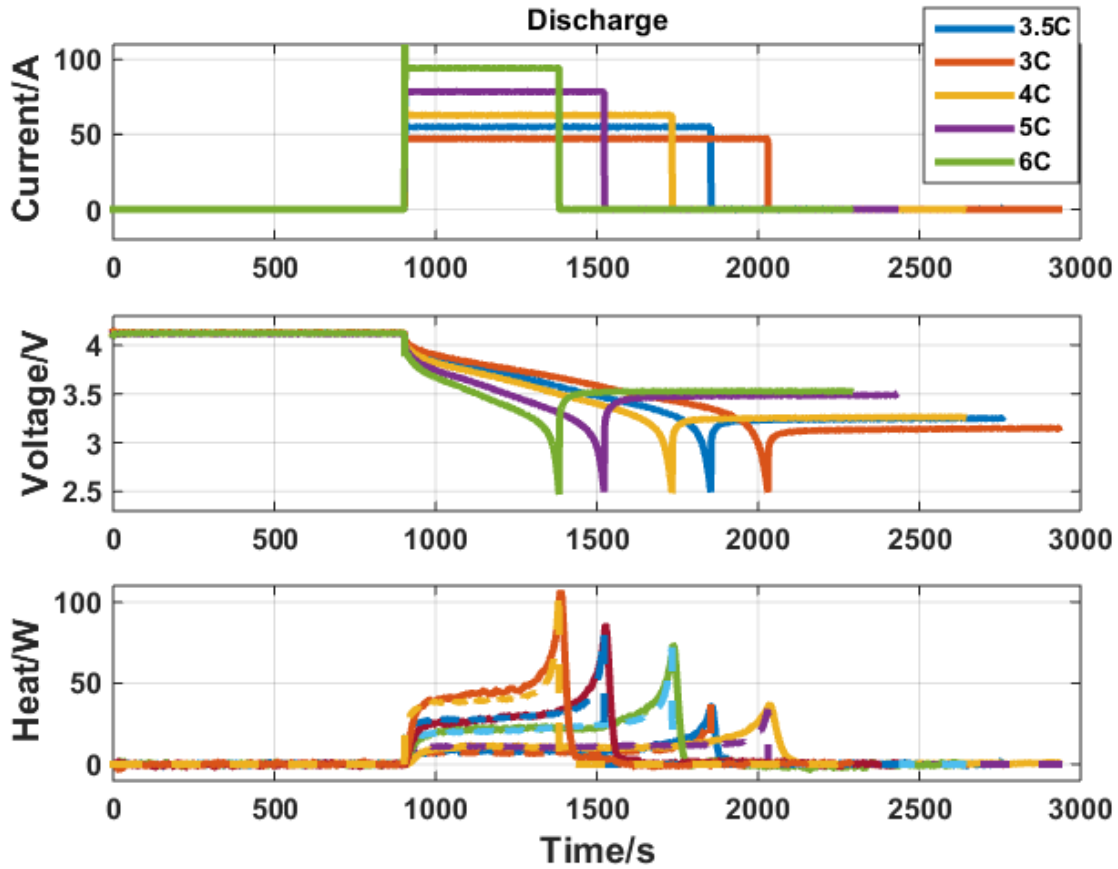


Figure 43: Heat generation of the battery during discharge

The current, terminal voltage and heat generation rate of the fresh battery is shown in Figure 43. The experimental data matches the calculation results well. The heat generation rate at the end of discharging rises more rapidly than at the beginning of the charging. In fact, the terminal voltage drops drastically when the battery is at low SOC, and the lithium-ion concentration gradient at the end of discharging is much higher than at the beginning, which causes the over-potential resistance to increase. The performance of the calorimeter is shown in Figure 44.

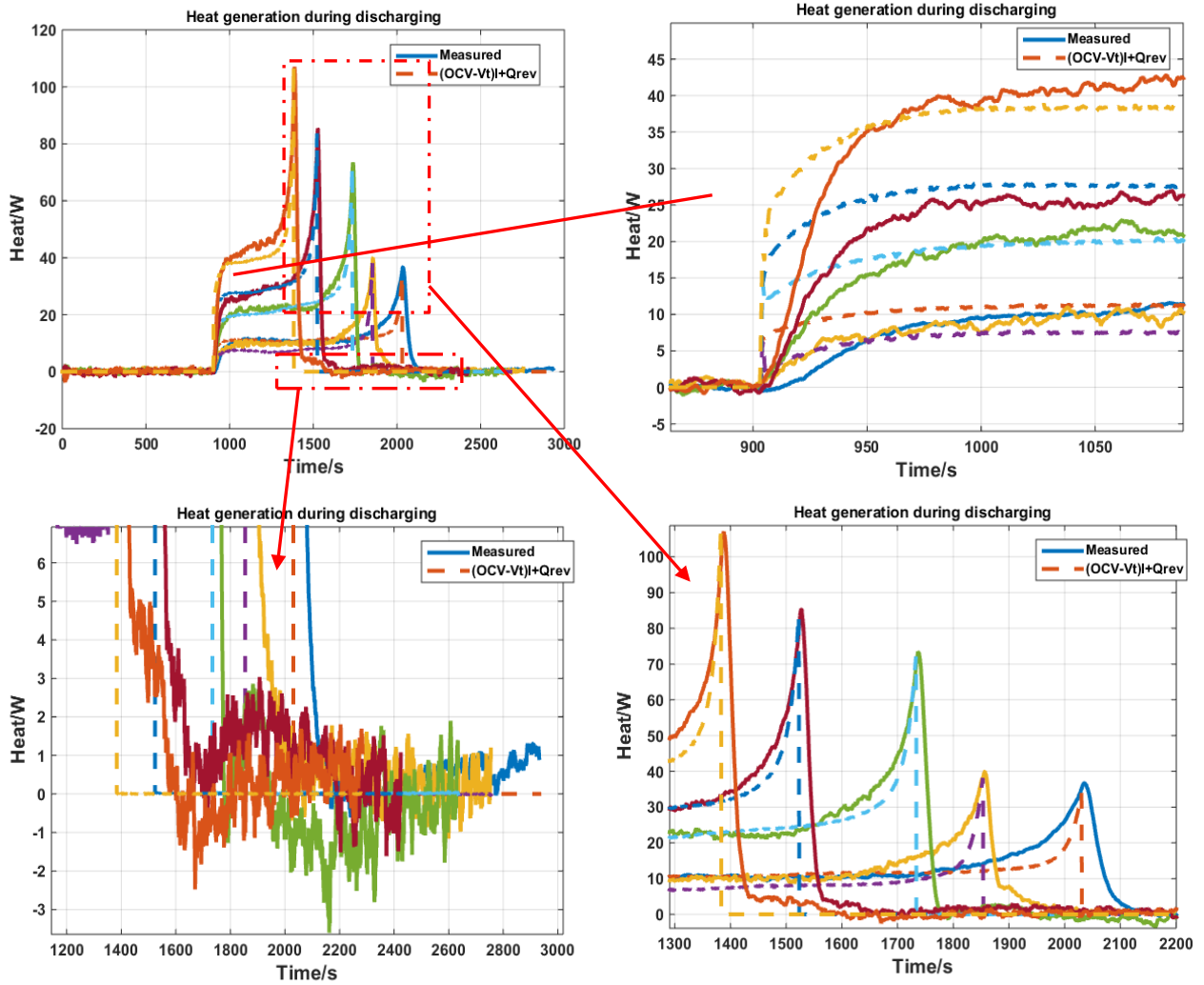


Figure 44: Performance of the calorimeter at discharging

The solid lines show the heat generation rate measured by the calorimeter; it takes around 60 seconds to follow the calculation results. When comparing 3C to 3.5C discharging rate, the measured data do not have much difference. However, based on the calculation, 3.5C discharge rate generates around 11W heat generation rate; 3C discharge rate generates around 7W heat generation rate. This is because the accuracy of the calorimeter is about 2W, when the heat generation rate is under 10W, the estimated error could be more than 20%. So this is a disadvantage of the designed calorimeter: it cannot measure heat generation rate precisely at the low heat generation rate (under 10W). In addition; the calorimeter measures about 5 watts of heat generation

rate of the battery at 6C discharging rate when the current is cut off. Even though the designed calorimeter has a time delay, from the zoomed-in figure, the heat generation rate drops sharply from 110W to 5W, and then it decays to zero in about 120 seconds. The period that the heat generation rate decays generally can be the heat of mixing which the theory calculation does not consider. This kind of heat can be neglected during charging but is significant after the current is interrupted.

The charging behavior of the battery is shown in Figure 45.

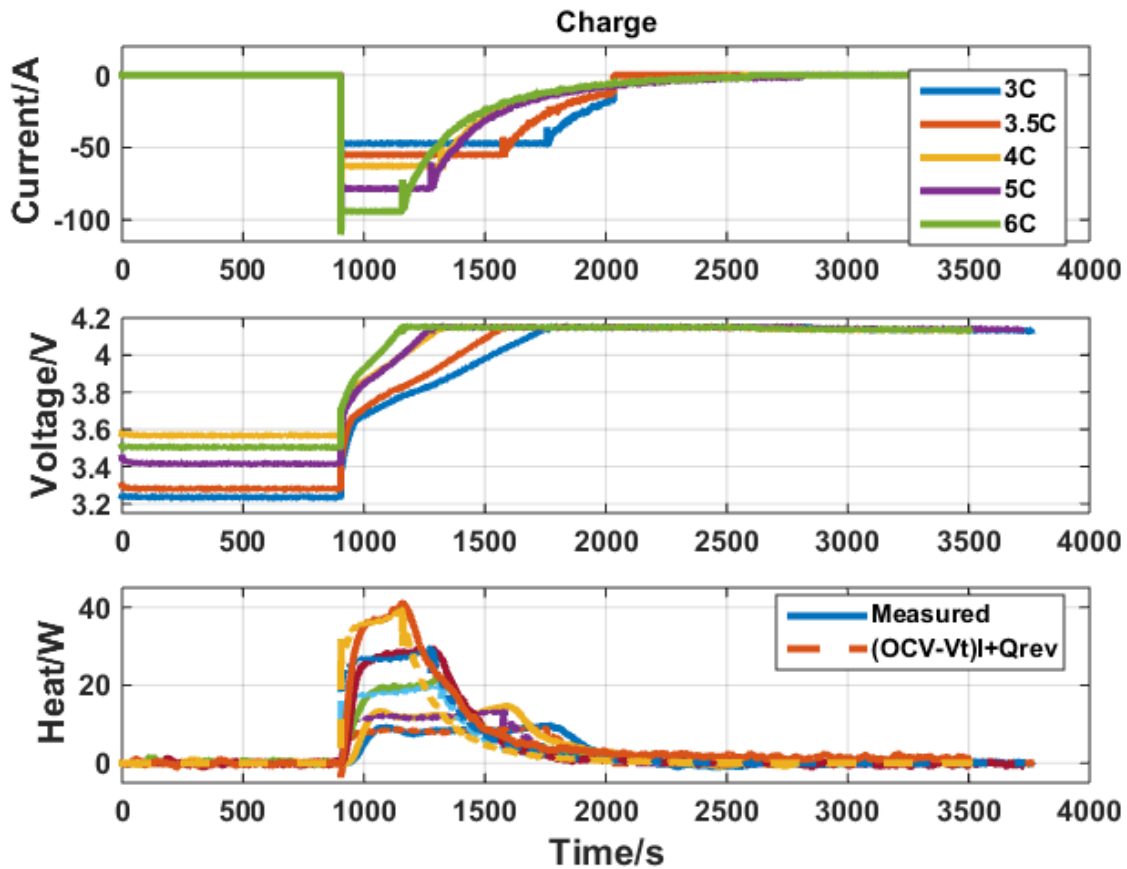


Figure 45: Heat generation of the battery during charge

The heat generation of the battery at the end of charging is much smaller than the discharging. However, the heat generation is almost the same between charging and discharging at the beginning. This is due to the reversible heat absorbs heat when the battery is charging and the

terminal voltage of the battery rises generally. From the OCV-SOC curve mentioned in the earlier of the study, the curve performs almost linearly between 100%-20%. In CC mode, SOC increases approximate linearly causing the OCV increases approximate linearly. Therefore, the OCV increases gently means there is no drastic change of the difference between the OCV and the voltage terminal voltage, which causing the heat generation rate at the end of charging is much smaller than the discharging. More details of the measurement heat generation during charging are shown in Figure 46

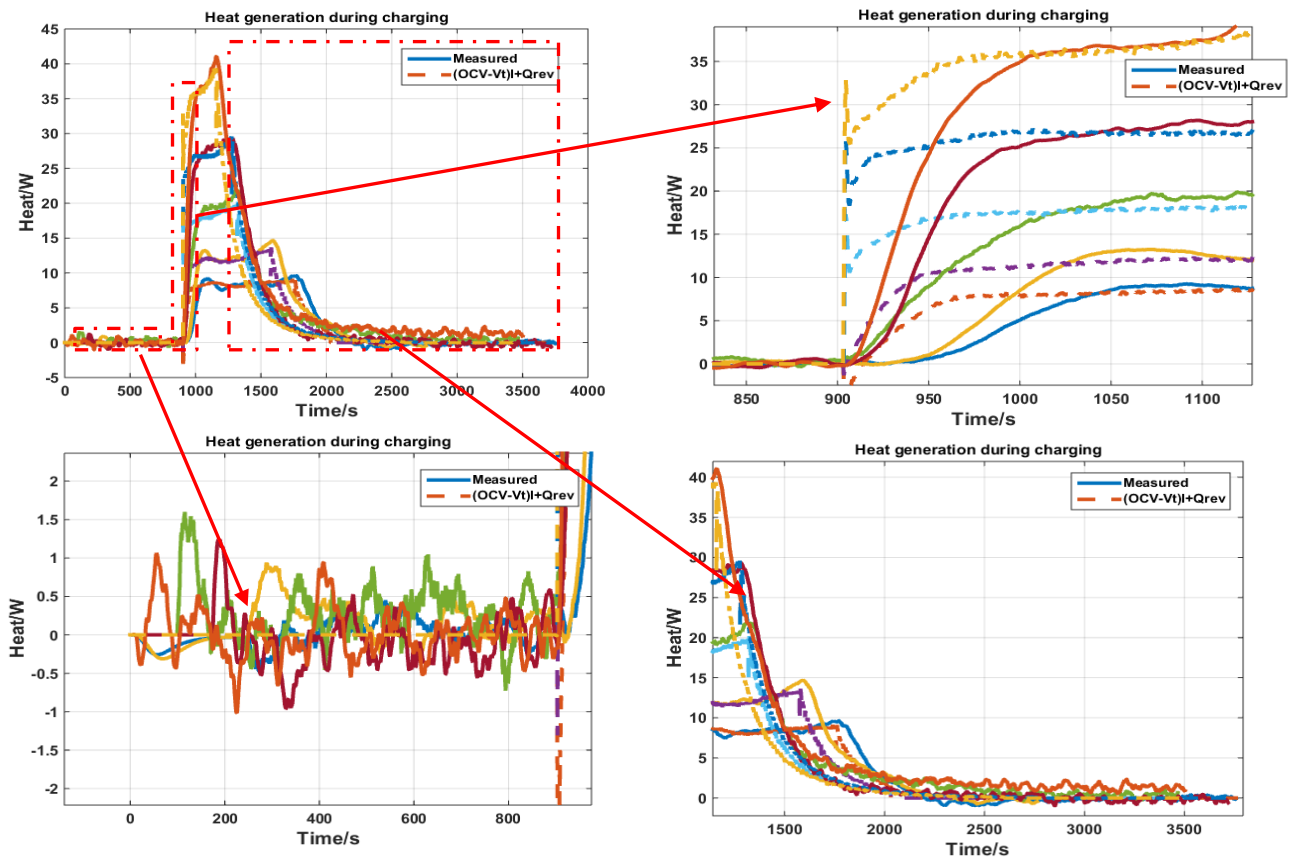


Figure 46: Performance of the calorimeter at charging

Before charging the battery, there should be no heat generation, but some caused by the error, a 1.5W calorimeter error. This is mainly caused by the input of the calorimeter: temperature and

current. The measured temperature has a 0.1 °C fluctuation, and the measured current has a 0.1A fluctuation. The fluctuation is caused by noises during measurements.

The response time becomes around 100s due to the increase of measurement covariance in Kalman filter. Because during charging the battery, the heat generation measurement range becomes smaller, the accuracy of KF needs to be improved. Increasing measurement covariance means trusting less in the measurement data and increases confident in the mathematical model. This action makes the measurement data smooth but needs more time to converge. When the charging model enters in CV mode, the terminal voltage of the battery maintains at 4.15V, and the current becomes smaller and smaller. In the period, heat generation of the battery decreases gently to zero.

5. Conclusion and future work

5.1. Conclusion

The coefficients of the heat pump rate, Joule heating, and heat conduction of the TEM are identified. The heat conductivity and capacity of the metal plate are also specified. A thermal model is built based on the determined parameters and the validation indicates that the parameters are close to the true value. The controller of temperature for the calorimeter is designed and optimized. The calorimeter can track a large step heat generation within 120 seconds and the steady state error is less than 5%. The calculation and measurement results are compared and show that the heat generation rate at the end of the discharging rises more rapidly than any other period of the whole charging. This is because the irreversible heat generation increases rapidly due to the open circuit voltage dropping drastically at the low SOC.

5.2. Future work

1. The ambient temperature of the calorimeter is not being controlled when the calorimeter is calibrated. The ambient temperature can affect the heat dissipation from the heat sink to the environment that may cause static calibration to be inaccurate, and the high ambient temperature can decrease the heat pump rate efficiency of the thermal electric module.
2. The method to calculate the heat generation rate of the lithium-ion battery does not consider the heat of mixing. Even though, it can be neglected at low C rates. Therefore, a new method needs to be developed to calculate the heat generation rate of the battery theoretically.
3. The calorimeter cannot maintain the surface temperature and measure the heat generation rate of the battery at the same time due to the metal plate. The passive load (heat

dissipation rate to the environment) of the metal plate needs to be determined, which enables to achieve two measurements simultaneously.

References

- [1] D. Linden and T. B. Reddy, Handbook of Batteries, Mc Graw-Hill Professional , 2001.
- [2] L. Song and J. W. Evans, "Electrochemical-Thermal Model of Lithium Polymer Batteries," *Journal of The Electrochemical Society*, vol. 147, no. 6, pp. 2086-2095, 2000.
- [3] M. Xiao and S.-Y. Choe, "Dynamic modeling and analysis of a pouch type LiMn2O4/Carbon high power," *Journal of Power Sources*, vol. 218, pp. 357-367, 2012.
- [4] Worldbank, "Lithium-ion Battery Overview," 2012.
- [5] T. Eriksson, "LiMn2O4 as a Li-Ion Battery Cathode," Uppsala University, UPPSALA, 2001.
- [6] J. Vetter, P. Novak, M. Wagner, C. Veit, K.-C. Moller, J. Besenhard, M. Winter, M. Wohlfahrt-Mehrens, C. Vogler and A. Hammouche, "Ageing mechanisms in lithium-ion batteries," *Journal of Power Sources*, vol. 147, p. 269–281, 2005.
- [7] S. Santhanagopalan, Q. Zhang, K. Kumaresan and R. E. White, "Parameter Estimation and Life Modeling of Lithium-Ion Cells," *Journal of The Electrochemical Society*, vol. 155, no. 4, pp. A345-A353, 2008.
- [8] G. G. Botte, V. R. Subramanian and R. E. White, "Mathematical modeling of secondary lithium batteries," *Electrochimica Acta*, vol. 45, p. 2595–2609, 2000.
- [9] D. D. MacNeil, Z. Lu, Z. Chen and J. R. Dahn, "A comparison of the electrode/electrolyte reaction at elevated temperature for various Li-ion battery cathode," *Journal of Power Sources*, vol. 108, p. 8–14, 2002.
- [10] J. Fan and S. Tan, "Studies on Charging Lithium-Ion Cells at Low Temperatures," *Journal of The Electrochemical Society*, vol. 153, no. 6, pp. A1081-A1092, 2006.

- [11] M. Ouyang, Z. Chu, L. Lu, J. Li, X. Han, X. Feng and G. Liu, "Low temperature aging mechanism identification and lithium deposition in a large format lithium iron phosphate battery for different charge profiles," *Journal of Power Sources*, vol. 286, pp. 309-320, 2015.
- [12] A. Awarke, M. Jaeger, O. Oezdemir and S. Pischinger, "Thermal analysis of a Li-ion battery module under realistic EV operating conditions," *International Journal of Energy Research*, vol. 37, pp. 617-630, 2013.
- [13] X. Zhao, G. Zhang, L. Yang, J. Qiang and Q. Chen, "A new charging mode of Li-ion batteries with LiFePO₄/C," *Journal of Thermal Analysis and Calorimetry*, vol. 104, p. 561–567, 2011.
- [14] K. Chen, G. Unsworth and X. Li, "Measurements of heat generation in prismatic Li-ion batteries," *Journal of Power Sources*, vol. 261, pp. 28-37, 2014.
- [15] J.-S. Hong, H. Maleki, S. A. Hallaj, L. Redey and J. R. Selmon, "Electrochemical-Calorimetric Studies of Lithium-Ion Cells," *Journal of the Electrochemical Society*, vol. 145, no. 5, pp. 1489-1501, 1998.
- [16] S. A. Hallaj, J. Prakash and J. Selman, "Characterization of commercial Li-ion batteries using electrochemical–calorimetric measurements," *Journal of Power Sources*, vol. 87, pp. 186-194, 2000.
- [17] J.-S. Kim, J. Prakash and J. R. Selman, "Thermal Characteristics of Li_xMn₂O₄ Spinel," *Electrochemical and Solid-State Letters*, vol. 4, pp. A141-A144, 2001.
- [18] C. Forgez, D. V. Do, G. Friedrich, M. Morcrette and C. Delacourt, "Thermal modeling of a cylindrical LiFePO₄/graphite lithium-ion battery," *Journal of Power Sources*, vol. 195, p. 2961–2968, 2010.

- [19] K. Yang, J. An and S. Chen, "Temperature characterization analysis of LiFePO₄/C power battery during charging and discharging," *Journal of Thermal Analysis and Calorimetry*, pp. 515-521, 2010.
- [20] D. Bernardi, E. Pawlikowski and J. Newman, "A General Energy Balance for Battery Systems," *Journal of the Electrochemical Society*, vol. 132, pp. 5-12, 1985.
- [21] W. B. Gu and C. Y. Wang, "Thermal-Electrochemical Modeling of Battery Systems," *Journal of The Electrochemical Society*, vol. 147, pp. 2910-2922, 2000.
- [22] G. Ciccarella and P. Marietti, "Model Reference Adaptive Control of a Thermostatic Chamber," *IEEE Transactions on Industrial Electronics*, vol. 36, pp. 88-93, 1989.
- [23] J. Schutze, H. Ilgen and W. R. Fahrner, "An Integrated Micro Cooling System for Electronic Circuits," *IEEE Transactions on Industrial electronics*, vol. 48, pp. 281-285, 2001.
- [24] M. Hodes, "Optimal Pellet Geometries for Thermoelectric Refrigeration," *IEEE Transactions on Components and Packaging Technologies*, vol. 30, pp. 50-58, 2007.
- [25] P. G. Lau and R. J. Buist, "Temperature and Time Dependent Finite-element Model of A Thermoelectric Couple," *IEEE Fifteenth International Conference on Thermoelectrics*, pp. 227-233, 1996.
- [26] W. Seifert, M. Ueltzen, C. Strumpel, W. Heiliger and E. Muller, "One-Dimensional Modeling of a Peltier Element," *IEEE Twentieth International Conference on Thermoelectrics*, pp. 439-443, 2001.
- [27] M. Guiatni, A. Drif and A. Kheddar, "Thermoelectric Modules: Recursive non-linear ARMA modeling, Identification and Robust Control," *The 33rd Annual Conference of the IEEE Industrial Electronics Society (IECON)*, pp. 568-573, 2007.

- [28] M. S. Grewal and A. P. Andrews, Kalman Filtering Theory and Practice Using MATLAB, Hoboken: John Wiley and Sons, 2008.
- [29] R. Fu, S.-Y. Choe, V. Agubra and J. Fergus, "Modeling of degradation effects considering side reactions for a pouch type Li-ion polymer battery with carbon anode," *Journal of Power Sources*, vol. 261, pp. 120-135, 2014.
- [30] X. Zhang, A. M. Sastry and W. Shyy, "Intercalation-Induced Stress and Heat Generation within Single Lithium-Ion Battery Cathode Particles," *Journal of The Electrochemical Society*, vol. 155, pp. A542-A552, 2008.